

1 Analysis of the 1 December 2011 Wasatch downslope windstorm

2 JOHN LAWSON * AND JOHN HOREL

Department of Atmospheric Science, University of Utah, Salt Lake City, Utah, United States of America.

* Corresponding author address: John Lawson, Department of Geological and Atmospheric Science, Iowa State University, Ames, IA 50011.

E-mail: john.rob.lawson@googlemail.com

ABSTRACT

A downslope windstorm on 1 December 2011 led to considerable damage along a narrow 50-km swath at the western base of the Wasatch Mountains in northern Utah. The strongest surface winds began suddenly at 0900 UTC, primarily in the southern portion of the damage zone. Surface winds reached their peak intensity with gusts to 45 m s^{-1} at $\sim 1600 \text{ UTC}$, while the strongest winds shifted later to the northern end of the damage swath. The northward shift in strong surface winds relates to the rotation of synoptic-scale flow from northeasterly to easterly at crest level, controlled by an evolving anticyclonic Rossby-wave-breaking event. A rawinsonde released at $\sim 1100 \text{ UTC}$ in the midst of strong ($>35 \text{ m s}^{-1}$) easterly surface wind intersected a rotor and sampled the strong inversion that surmounted it.

The windstorm's evolution was examined further via Weather Research and Forecasting model simulations initialized from North American Mesoscale analyses $\sim 54 \text{ h}$ before the windstorm onset. The control model simulation captured core features of the event, including the spatial extent and timing of the strongest surface winds. However, the model developed stronger mountain-wave breaking in the lee of the Wasatch, a broader zone of strong surface winds, and a downstream rotor located farther west than observed. A second simulation, in which the nearby east–west-oriented Uinta mountains were reduced in elevation, developed weaker easterly flow across the Wasatch during the early stages of the event. This result suggests that the Uinta Mountains block and steer the initial northeasterly flow across the Wasatch.

²³ 1. Introduction

²⁴ Downslope windstorms arise when a layer of air is sandwiched between a terrain bar-
²⁵ rier and a strongly-stable layer aloft, while being forced over the barrier (Markowski and
²⁶ Richardson 2010). Due to the damage often associated with downslope windstorms, they
²⁷ have obtained local names in areas experiencing them frequently, including the föhn, bora,
²⁸ chinook, zonda, Santa Ana, and Wasatch (Whiteman 2000; Richner and Hächler 2013).
²⁹ As discussed by Richner and Hächler (2013), the general synoptic features associated with
³⁰ localized downslope windstorms are well understood and reasonably well predicted.

³¹ The Wasatch windstorm of 1 December 2011 caused over \$75 million damage in a narrow
³² swath, roughly 3–5 km wide and 50 km long as delineated by the hatched rectangular box
³³ in Fig. 1a along the Wasatch Front (O'Donoghue 2012). The Wasatch Front describes the
³⁴ urban–suburban corridor paralleling the west slopes of the Wasatch Mountains. Impacts of
³⁵ this storm, which was later declared a federal disaster, included: as many as 70,000 trees
³⁶ were uprooted or damaged; power was lost in many communities after over 22 transformers
³⁷ were damaged and 1.5 km of power lines required maintenance; rail traffic was halted along
³⁸ the Wasatch Front; and Interstate 15 was closed to large vehicles after many were blown
³⁹ over on the freeway.

⁴⁰ An anemometer sited by Union Pacific Railroad in Centerville, UT, along a stretch of rail
⁴¹ line prone to high winds during downslope windstorms, recorded a maximum gust of 45 m s^{-1}
⁴² (102 mph) at $\sim 1600 \text{ UTC}$ ¹ 1 December 2011 (Fig. 2). Strong winds were not only observed
⁴³ along the Wasatch Front on this day, but also in other localized areas across the western
⁴⁴ United States; for example, southern California experienced one of its strongest Santa Ana
⁴⁵ events in recent years (Welch and Rice 2011).

⁴⁶ Forecasting the occurrence of downslope windstorms has long been recognized to re-
⁴⁷ quire several critical ingredients (Smith 1985; Markowski and Richardson 2010). Follow-
⁴⁸ ing Markowski and Richardson (2010), the terrain barrier must first be: (1) quasi-two-

¹Local time in Utah is 7 h earlier than UTC during winter.

dimensional so that air cannot simply flow around it, and (2) asymmetrical with a more gentle windward slope combined with a steep lee slope (Miller and Durran 1991). However, no single terrain characteristic is tied to strong-windstorm environments. Figure 2 depicts the steep lee-side profile along the Wasatch Front, near Centerville, UT. Here, the flat base of elevation 1280 m above mean sea-level rises eastward towards the crest of the Wasatch mountains (2500–2750 m in this region).

Second, a sufficiently-strong cross-barrier wind ($>15 \text{ m s}^{-1}$) must impinge on the barrier; a wind direction orthogonal to a two-dimensional barrier will maximize the cross-product of the crest orientation and wind direction, and hence mountain wave excitation in the same direction downstream. Third, the vertical profiles of temperature, moisture, and wind should be conducive to amplifying the development of mountain lee waves. This typically requires one or more of the following characteristics: (1) a strongly-stable layer upstream of and above the crest level (Vosper 2004); (2) an environmental critical level above crest level, where the cross-wind component decreases to zero and/or reverses direction (e.g., Wang and Lin 1999); (3) a wave-induced critical level (Peltier and Clark 1979), where wave-breaking itself generates a wind reversal above crest level that is not found in upstream wind profiles; or (4) the synoptic environment should favor subsidence aloft, but not favor the development of a deep cold-air pool in the lee of the range that might inhibit penetration of strong winds to the surface (Jiang and Doyle 2008).

National Weather Service (NWS) forecasts issued by the Salt Lake City Forecast Office for the 1 December 2011 Wasatch windstorm were ample for public and private contingency planning in terms of spatial and temporal accuracy, forecast lead time, and wind speed magnitude. The first Area Forecast Discussion (AFD) to mention a potential for strong winds along the Wasatch Front on 1 December was issued at 1712 UTC 27 November (90 h before the onset of the windstorm) and the matter was discussed in the subsequent Hazardous Weather Outlook (HWO). All further AFDs and HWOs issued by the Salt Lake City Forecast Office mentioned the chance for high winds, with increasing confidence as the event drew

76 closer. The potential for high winds was cited in many AFDs to be based on: (1) the
77 similarity between the developing synoptic situation and situations observed during prior
78 major Wasatch windstorms, and (2) confidence in both the numerical model guidance from
79 operational forecast models and a higher-resolution model run locally at the Forecast Office
80 ².

81 Planning for this study began the day before the windstorm, and was motivated by
82 a number of factors: (1) operational numerical guidance and forecaster experience led to
83 high confidence that a major downslope windstorm was possible; (2) verification of this
84 forecast would lead to the first major downslope windstorm along the Wasatch Front in over
85 a decade; (3) experimental high-resolution numerical forecasts run by the Salt Lake City
86 National Weather Service Office were providing considerable specificity regarding the details
87 of the impending windstorm; and (4) routine automated observations were already in place
88 throughout the region such that additional observational assets available in the Department
89 of Atmospheric Sciences could be used advantageously to mount a small field campaign to
90 study the event (the equipment available has been described by Lareau et al. 2013). On
91 30 November, a University of Utah (UoU) team quickly drew up a research plan to collect
92 additional observations the next day using surface weather stations, portable rawinsonde
93 systems, and vehicle-mounted sensors. While a major downslope windstorm was deemed
94 likely by forecasters, and supported by high-resolution deterministic model output, UoU
95 team confidence was not particularly high regarding the specific details (timing, location,
96 and intensity) of the high-resolution numerical guidance provided by the NWS.

97 The resulting severity of the event, combined with the accuracy of the high-resolution
98 model guidance, the apparent extended predictability, and an unprecedented data set for a

²Weather Research and Forecasting mesoscale model runs were made four times a day with boundary conditions based on the prior Global Forecast System model. The regional domain was 12 km, and nested down to 4 km across Utah. Each run produced hourly guidance through 60 forecast hours. This was the first major Wasatch windstorm where forecasters had access to high-resolution forecast guidance in their operational office environment (Randy Graham and Steve Rogowski, 2012, personal communication).

99 Wasatch downslope windstorm, ultimately led to completion of this study. Our objectives
100 are to examine the 1 December 2011 Wasatch downslope windstorm from several distinct
101 perspectives: (1) relate briefly this event to previous downslope windstorms; (2) analyze
102 the spatial and temporal evolution of the winds on the basis of local observations from
103 conventional sources and those collected specifically during the small field campaign; (3)
104 evaluate a high-resolution model simulation in terms of its ability to resolve the mesoscale
105 and local features of the event; and (4) assess the impacts of the upstream Uinta Mountains
106 that may deflect the flow traveling towards the Wasatch Mountains. Lawson (2013) provides
107 additional details about this research.

108 **2. Data and Model Configuration**

109 *a. Observational data*

110 Surface observations of meteorological and other environmental parameters were obtained
111 from the MesoWest archive (Horel et al. 2002b). Reports from over 280 automated reporting
112 stations were available within 80 km (50 mi) of Centerville, UT, the location of the strongest
113 winds on 1 December 2011. There are substantive differences in the siting, equipment,
114 and reporting characteristics of the automated observations available in MesoWest. Wind
115 observations were manually evaluated to identify the time and intensity of the strongest
116 observed winds.

117 An ad hoc UoU team of staff and students assembled during the morning of 30 November
118 to determine where additional observations would best improve evaluation of
119 the expected windstorm. Decisions were made and implemented that afternoon to deploy
120 three automated weather stations (locations shown in Fig. 1b): (1) near Morgan, UT, im-
121 mediately east of the Wasatch Range and located roughly along the cross section shown in
122 Fig. 1 to monitor conditions upstream of the Wasatch; (2) east of Bountiful, UT, \sim 500 m
123 in elevation above the foot of the slope and as far up as it was practical to drive given the

¹²⁴ weather and mountain road conditions; and (3) Glover's Lane (MesoWest identifier UFD04)
¹²⁵ in Farmington, UT, ~1.5 km west of the base of the Wasatch. Two mobile Graw rawinsonde
¹²⁶ systems were prepared for the next day: one to be sited where the portable automated
¹²⁷ weather station was deployed near Morgan, UT (upstream of the Wasatch Mountains); the
¹²⁸ other to be deployed as needed in the lee of the range based on how the conditions evolved.
¹²⁹ Two vehicles were also equipped with roof-mounted GPS, wind, temperature, humidity, and
¹³⁰ pressure sensors. However, one of the roof-mounted racks was destroyed early the next day
¹³¹ in the high winds.

¹³² *b. Model setup*

¹³³ Numerical simulations were performed with the Weather Research and Forecasting (WRF)
¹³⁴ model, version 3.4, using the Advanced Research WRF dynamical core. All runs comprised
¹³⁵ three nested domains of grid size 12, 4, and 1.3 km (Fig. 3), whose initial and boundary
¹³⁶ (updated every 6 h) conditions were provided by the North American Mesoscale model. The
¹³⁷ domains allowed two-way feedback; high-frequency waves were damped with sixth-order dif-
¹³⁸ fusion on the largest domain. Topography was interpolated from datasets at a resolution of
¹³⁹ 10 min for the 12-km domain, and 30 s for the 4- and 1.33-km domains, to the WRF-model
¹⁴⁰ grids. To avoid Courant-Friedrichs-Lowy criterion violation in regions of active mountain-
¹⁴¹ wave breaking, vertical resolution was limited to 40 vertical levels. WRF output was in-
¹⁴² terpolated onto a pressure-coordinate grid. Further details and parametrization options are
¹⁴³ listed in Table 1.

¹⁴⁴ **3. Results**

¹⁴⁵ *a. Climatology*

¹⁴⁶ Windstorms along the Wasatch Front (Fig. 1) occur in climatologically-anomalous east-
¹⁴⁷ erly flow at crest level (Holland 2002; Horel et al. 2002a). Easterly windstorms (Mass and
¹⁴⁸ Albright 1985; Jones et al. 2002, e.g.,) are hence rarer than those that occur on lee slopes
¹⁴⁹ downwind of prevailing midlatitude westerly flows (Lilly and Zipser 1972; Zhong et al. 2008,
¹⁵⁰ e.g.,). As discussed by Holland (2002), few meteorological surface stations in the vicinity
¹⁵¹ of the Wasatch Mountains are located in appropriate locations or have extensive enough
¹⁵² records to develop climatologies of Wasatch windstorms. For example, the Salt Lake Inter-
¹⁵³ national Airport (KSLC in Fig. 1) is too far west of the range and does not experience strong
¹⁵⁴ downslope winds during these events.

¹⁵⁵ Following Holland (2002), observations from Hill Air Force Base (KHIF, Layton, UT in
¹⁵⁶ northern Davis County) are used to examine the occurrence of strong downslope winds
¹⁵⁷ between 1 October 1979 and 30 April 2012, the period for which European Centre for
¹⁵⁸ Medium-Range Weather Forecasts (ECMWF) Re-Analysis (ERA)-Interim data are avail-
¹⁵⁹ able (Dee et al. 2011). Of observation stations that experience windstorms (i.e. that are
¹⁶⁰ close to the base of the Wasatch), KHIF has the longest and most reliable record. Due to
¹⁶¹ its position 5 km west of the Wasatch Front base, and near the exit of Weber Canyon, KHIF
¹⁶² frequently experiences easterly drainage flows in addition to occasional downslope wind-
¹⁶³ storms (Chrast et al. 2013). Holland (2002) found easterly wind gusts $>23 \text{ m s}^{-1}$ about 1.5
¹⁶⁴ times per year during the period 1953–1999, with more events observed in the earlier years
¹⁶⁵ than the later ones. Over time, there has been suburban development near KHIF, but not
¹⁶⁶ substantial enough to be responsible for the lower frequency of events in these later years.
¹⁶⁷ The strongest wind gust recorded at KHIF was 45 m s^{-1} on 4 April 1983. Holland (2002)
¹⁶⁸ derived composites of geopotential height on standard pressure levels for 79 strong easterly
¹⁶⁹ wind events using coarse-resolution (2.5° latitude/longitude grid) National Centers for En-

¹⁷⁰ vironmental Prediction/National Center for Atmospheric Research reanalyses. Consistent
¹⁷¹ with synoptic experience and forecasting practices at that time, the dominant composite
¹⁷² signal described in that study was the development of a closed geopotential-height low on
¹⁷³ the 700-hPa surface, southwest of the Wasatch Mountains and centered near Las Vegas, NV.
¹⁷⁴ Receiving less attention in that study was the development to the north of the Wasatch
¹⁷⁵ Mountains of a composite geopotential-height ridge at 700 hPa, which extended from coastal
¹⁷⁶ Washington state, curving through Montana, to Wyoming. This cyclone–anticyclone struc-
¹⁷⁷ ture is consistent with the life-cycle 1 (LC1) type of Rossby-wave breaking (Thorncroft et al.
¹⁷⁸ 1993), i.e., anticyclonic Rossby-wave breaking (ARWB).

¹⁷⁹ A more conservative definition for strong Wasatch windstorms than that applied by
¹⁸⁰ Holland (2002) is used in this study. A high wind event between October and April in-
¹⁸¹ clusive must satisfy the following criteria: (1) at least one KHIF observation with greater
¹⁸² than 15 m s^{-1} sustained winds from an easterly direction between 45° and 135° ; and (2)
¹⁸³ ERA-Interim analyses must indicate a Rossby wave-breaking pattern (either anticyclonic as
¹⁸⁴ described above, or cyclonic LC2 type with a trough or closed low tilting in the east- and
¹⁸⁵ poleward direction, Thorncroft et al. 1993). One strong easterly-wind event at KHIF met
¹⁸⁶ criterion (1), but not (2), and was ignored. In addition, multiday events were reduced to
¹⁸⁷ a single day if they were associated with the same upper-level wave-breaking event. These
¹⁸⁸ criteria led to identification of 13 distinct downslope windstorms between 1 October 1979
¹⁸⁹ and 30 April 2012 inclusive. Table 2 shows their dates and sustained speeds and wind gusts.

¹⁹⁰ The list of dates in Table 2 and the time series of their occurrence during 1979–2012
¹⁹¹ (Fig. 4) suggests that major downslope windstorms occurred once or twice every few years
¹⁹² until 1999. Subsequently, no major downslope windstorm occurred until the 1 December 2011
¹⁹³ event investigated here. The intermittency of Wasatch windstorms, particularly the lack of
¹⁹⁴ windstorms in the first decade of this century, raises the question whether their occurrence
¹⁹⁵ is determined by fewer Rossby-wave breaking events over western North America, or more
¹⁹⁶ directly, by fewer crest-level easterly wind periods during winter. Strong and Magnusdottir

197 (2008) developed an objective detection algorithm that generated a worldwide Rossby-wave-
198 breaking climatology. Perhaps because their criteria allowed for weak and localized wave-
199 breaking events, examination of their data as part of this study did not yield an obvious
200 linkage of ARWB events to the occurrence of Wasatch windstorms. Figure 4 also shows
201 the frequency of easterly (between 45° and 135°) crest-level (700 hPa) winds over 10 m s^{-1}
202 during each winter season (October–April inclusive) from the ERA Interim Reanalyses. Since
203 crest-level strong-easterly-wind periods do occur in the years that downslope windstorms
204 were absent, the seasonal frequency of easterly winds is not a good predictor for the rare
205 occurrences of downslope windstorms within those seasons. Hence, we can offer no definitive
206 explanation for the absence of major Wasatch downslope windstorms during the 2000–2010
207 period.

208 In our set of 13 major windstorms (Table 2), the hour of peak wind at KHIF varies
209 from 0700 UTC to 1800 UTC. In general, the peak in widespread downslope winds along
210 the Wasatch Front tend to occur near sunrise (~ 1200 UTC), since the dynamical forcing
211 associated with the downslope winds is in phase at that time with thermally-forced drainage
212 flows down slopes and valleys (Chrast et al. 2013). Hence, similar to Holland (2002), we
213 show in Fig. 5 composites of 700-hPa geopotential height, assuming that the peak downslope
214 wind occurs near 1200 UTC, and then composite conditions from 12 h earlier (0000 UTC) to
215 6 h after (1800 UTC). Southeastward progression of the tighter geopotential-height gradient
216 associated with the breaking anticyclonic wave (e.g., Fig. 5b) marks the ARWB event, while
217 the associated closed low deepens from 0000 to 1200 UTC followed by filling. The strongest
218 easterly gradient winds across the Wasatch Front are at 1200 UTC.

219 In this climatological context, we find the windstorm of 1 December 2011 to be not only
220 one of the strongest on record, but also the first in over ten years to match our criteria.
221 In the next two subsections, we present observational and modeling data, respectively, to
222 address why this was such a rare and damaging event.

223 b. 1 December 2011 windstorm

224 Figure 6 summarizes the synoptic evolution of the ARWB event on 1 December 2011 in
225 ERA-Interim geopotential height and wind data on the 700-hPa surface. A small southwest-
226 moving wave in the height field, accompanied by a jet maximum, moves faster than the
227 mean flow towards the base of the trough between 0000 and 1200 UTC. The transport of
228 cyclonic vorticity into the trough axis may contribute to the deepening of the closed low over
229 the Nevada–Utah–Arizona borders: 700-hPa heights drop 60 m between 0000 and 0600 UTC,
230 and fall another 30 m between 0600 and 1200 UTC. Lower-tropospheric cyclogenesis is often
231 seen with LC1 baroclinic waves (Thorncroft et al. 1993). The closed-low center does not
232 move far while its central height falls and the anticyclonic ridge breaks to the north. This
233 clockwise pivoting of the breaking wave, and its slow southeastward progression, sustained
234 a belt of 25 m s^{-1} easterly winds on the northwestern quadrant of the low-height center.
235 By 1200 UTC, the crest of the Wasatch Front (at $\sim 700 \text{ hPa}$) lies within this belt of strong
236 easterly flow.

237 A longitude–pressure cross-section of zonal wind and potential temperature, taken on
238 a west–east slice at 1200 UTC through ERA-Interim data, indicates a low-level easterly jet
239 surmounted by a statically-stable layer to the east of the Wasatch Front (not shown). Farther
240 aloft, cross-barrier flow reverses with height. As mentioned in section 1, both this elevated
241 stable layer and the flow reversal are conducive to initiation and amplification of mountain
242 waves.

243 The first northward mobile transect along the Wasatch Front between 0915 and 1015 UTC
244 captured the sudden onset of the strongest winds (Fig. 7). Departing from the UoU cam-
245 pus, strong easterly winds were first encountered south of Centerville (CENWWS) with the
246 peak winds found near Centerville. Strong easterly winds were also observed at the western
247 mouth of the Weber River Canyon while speeds dropped off substantially farther east up
248 the canyon. Union Pacific Railroad halted all train traffic at the eastern mouth of Weber
249 Canyon, the end of the mobile-sensor transects in Fig. 7. Temperature and pressure mo-

bile observations indicated near-uniform potential temperature at the base of the Wasatch Front; lower potential temperatures in the Weber River Canyon reflected the contribution of thermally-driven canyon flows to wind speed in this area (not shown). A 50-m tower located at the mouth of Weber River Canyon (Chrast et al. 2013) sampled winds at 3, 10, 30, and 50 m above ground level. Mean wind speeds generally increase with sensor height during the period of strongest winds (1100–1900 UTC, not shown). However, due to the turbulent nature of the combined exit and downslope flows, peak winds are roughly equivalent in the 10–50 m range; notably, 3-m wind gusts are occasionally as strong as those much farther aloft.

Figure 8a shows the time series of surface winds at KHIF on 1 December 2011 with most observations reported at hourly intervals. The strongest downslope winds were observed at this location during 1500–1800 UTC, preceded by a brief period of strong winds at 1200 UTC. Figure 8b shows wind speed and direction at Glover’s Lane (UFD04), a station installed temporarily in Farmington, UT the previous evening by the UoU team and located 1.5 km from the base of the Wasatch. The observations of wind speed and direction at 1-min intervals capture the sudden onset and cessation of the downslope windstorm at 0900 and 1900 UTC respectively, and show winds reaching their peak intensity at this location ∼1500–1600 UTC. These two stations (KHIF and UFD04) are representative of the windstorm’s characteristics along the foothills, including the time of peak winds occurring later farther north along the Wasatch Front. In contrast to the sudden onset and cessation of downslope winds in the valley, winds at the crest of the Wasatch as measured at Ogden Peak (OGP, Fig. 8c) show a persistent easterly flow with winds increasing in intensity until late afternoon.

Vertical profiles of wind, temperature, and moisture, collected by rawinsondes launched twice-daily at KSLC during prior windstorms, have exhibited primarily the prevailing synoptic flow combined with complex downstream effects of the flow over the Wasatch Range. Figure 9 shows the KSLC sounding launched at ∼1100 UTC with a nominal observation time of 1200 UTC. The profile exhibits features typically observed at KSLC during a Wasatch wind-

277 storm: (1) no indication of downslope winds near the surface (i.e., weak low-level southerly
278 drainage flow down the Salt Lake Valley towards the Great Salt Lake); (2) strong easterly
279 winds below and extending above crest level (700 hPa); (3) easterly winds weakening aloft
280 with limited cross-barrier flow at 500 hPa; (4) little moisture evident in the profile; (5) a
281 small surface-based inversion with a well-mixed layer extending upwards to \sim 750 hPa; (6)
282 evidence of strong turbulence between 750 and 700 hPa with superadiabatic lapse rates; and
283 (7) a capping inversion layer near crest (\sim 690 hPa) with an adiabatic layer above that level
284 to 650 hPa.

285 The UoU team planned to launch rawinsondes upstream and downstream of the Wasatch
286 at roughly the same time as the nearby NWS launch at KSLC (\sim 1100 UTC), and then to
287 continue operations as conditions warranted. These additional launches were intended to
288 describe the flows upstream and immediately downstream of the terrain where the strongest
289 winds were expected. Upstream launches near Morgan, UT were made at the nominal
290 observation times of 1200, 1500, and 1800 UTC (i.e., balloons released at 1100, 1400, and
291 1700 UTC, respectively). Since short-period communication failures between the radio base
292 station and the 1200 and 1500 UTC sondes near Morgan created small data gaps of 25–75 hPa
293 in depth, the 1800 UTC profile is shown in Fig. 10a. The automated algorithms provided
294 by the rawinsonde manufacturer tend to smooth excessively the wind observations, hence
295 the following figures use raw, unsmoothed wind data. Upstream of the Wasatch Range, the
296 lowest 750 m is well-mixed and nearly adiabatic, below a string of stable layers up to 5 km.
297 A particularly strong inversion is evident at \sim 3250 m, an elevation roughly 500 m above the
298 crest of the Wasatch in this area, which caps a layer with higher relative humidity and the
299 strongest easterly winds (\sim 30 m s $^{-1}$) observed at this time. Above the highest inversion,
300 winds are substantively weaker, and relative humidity is lower. Notably, easterly winds are
301 observed throughout the profile below 5000 m.

302 A day previously, the UoU team selected a park in Centerville, UT for a lee-side raw-
303 insonde launch. Fortuitously, its position was within the core of strongest wind observed

304 during the event, located immediately upwind (~ 200 m) of the UDOT tower (CEN) and
305 Union Pacific Railroad tower (CENWWS), themselves immediately west of the Interstate 15
306 freeway (see Fig. 2). Sound-barrier walls east of the freeway bracket the park on its north
307 and south edges and contributed to channeling of the flow. Several trucks tipped over as
308 they passed northward from the protection of the sound barrier into the unprotected zone
309 on the freeway, as well as on the adjacent frontage road. It was under these extremely
310 harsh conditions that the UoU team successfully launched a rawinsonde at 1100 UTC at the
311 park. The balloon initially travelled nearly horizontally towards the freeway, before gain-
312 ing altitude and clearing trees located at the edge of the frontage road. Vertical profiles of
313 potential temperature, relative humidity, and wind speed and direction from the 1200 UTC
314 Centerville sounding are shown in Fig. 10b. Two small communication gaps occurred during
315 the ascent, one at 3050–3200 m, and another at 3400–3500 m. The immediate surface layer
316 (lowest 50–60 m) is characterized by lower potential temperature and horizontal winds ap-
317 proaching 40 m s^{-1} , consistent with the nearby surface wind gust observations of $\sim 36 \text{ m s}^{-1}$
318 at CENWWS at this time. Following Armi and Mayr (2011), this layer is referred to as the
319 “downslope underflow”.

320 A sharp inversion (5.7°C increase in ~ 3.5 hPa) at 3300 m caps a turbulent layer con-
321 taining adiabatic, superadiabatic, and weakly stable sublayers between 1700 m and 3300 m.
322 Relative humidity increases to 90% through this depth and falls sharply through the in-
323 version. Winds again increase to over 30 m s^{-1} in the inversion layer, and rotate above the
324 inversion to sharply-reduced cross-barrier flow above 3750 m. This rotation is not evident
325 upstream near Morgan, and may therefore be self-induced. The sharp inversion is consis-
326 tent with flow separation as the air crosses the Wasatch; the downslope underflow descends
327 steeply along the slope, while another strong easterly current flows outward near crest level
328 (~ 3300 m). All three sondes upstream of the Wasatch Range detected the strongest winds
329 ($25\text{--}30 \text{ m s}^{-1}$) at 3100–3200 m, consistent with the strong crest-level winds observed near the
330 inversion layer above Centerville.

331 Figure 11 contrasts the ascent rates at \sim 1–2-s intervals experienced by the Morgan and
332 Centerville rawinsondes. The ascent rate near Morgan, averaged from surface to 3300 m, is
333 4.8 m s^{-1} , which is roughly what would be expected given the amount of helium used in the
334 balloon (e.g., the 1200 and 1500 UTC sondes had average ascent rates of 4.5 and 5.3 m s^{-1} ,
335 respectively). The Centerville rawinsonde, using a similar volume of helium, experienced
336 vastly different conditions from that near Morgan. Consistent with visual tracking of the
337 Centerville sonde until lost in the dark, the buoyancy imparted by the helium was initially
338 negated by descending motions, resulting in a near-horizontal trajectory. Then, the rawin-
339 sonde ascended at increasingly rapid rates approaching 25 m s^{-1} through the superadiabatic
340 layer. Vertical speeds then decreased up to 2900 m. The balloon made no headway verti-
341 cally through the sharp inversion, and at times descended in that layer, which led to a large
342 number of observations in this vicinity. Once clear of this layer, the balloon ascended at an
343 average rate of 4.6 m s^{-1} . Subtracting this mean ascent rate from the observed rate yields a
344 crude estimate of peak vertical velocities $O(20 \text{ m s}^{-1})$ upwards and $O(7.5 \text{ m s}^{-1})$ downwards.

345 The violent ascent and descent of the balloon is consistent with visual evidence after
346 sunrise of rotors (low-level vortices with horizontal axes parallel to the ridgeline in the lee of
347 mountain range; Doyle and Durran 2002). Satellite images and photos indicate an upstream
348 cloud deck over the Wasatch evaporating in the air descending down the lee slope with
349 distinctive rotor clouds evident to the west of the base of the slope (not shown). The quasi-
350 uniform horizontal distance from the crest to the location of the rotor clouds is \sim 10 km (3–
351 5 km from the base of the mountains). The superadiabatic lapse rate in the layer 2000–2500 m
352 may result from the formation of rotor clouds and then subsequent evaporative cooling of
353 the air when the clouds dissipate. Aircraft, dropsonde, and lidar observations from the
354 Terrain-Induced Rotor Experiment (T-REX) provide more comprehensive depictions of the
355 turbulence and rotors present in the lee of the Sierra Mountains during downslope windstorms
356 (Armi and Mayr 2011; Kühnlein et al. 2013). For example, aircraft and lidar observations
357 during T-REX detected vertical velocities greater than $10\text{--}15 \text{ m s}^{-1}$ in the ascending air

358 beneath rotor clouds.

359 *c. Control simulation*

360 The ability of a numerical simulation to capture the core features observed during this
361 windstorm is now examined. A numerical simulation, referred to as the Control simulation,
362 was performed with the WRF model initialized from the NAM-model analysis at 0600 UTC
363 29 November 2011, and forced thereafter on the outermost boundary by NAM analyses
364 updated every 6 h. The Control simulation is initialized far enough in advance for mesoscale
365 circulations to develop freely, and continues for 72 h to encompass the entire downslope
366 windstorm event. The simulated 700-hPa geopotential height fields for 0000–1800 UTC 1
367 December (42–60 h into the simulation) are shown in Fig. 12, taken from the largest (12-km)
368 WRF domain. The model captures the synoptic-scale structure of this ARWB event, with
369 a ridge developing and extending southeastward from northern Idaho into Wyoming, while
370 the cut-off low becomes centered near the southern tip of Nevada. Relative to the 700-hPa
371 circulation depicted in the ERA-Interim reanalyses, values of geopotential height simulated
372 by the model are elevated by \sim 60 m everywhere, but the modeled height gradients are similar
373 to those analyzed, particularly in the vicinity of the Wasatch Front. However, the model
374 simulation is slower in its development of the ARWB event, with the cut-off low-height center
375 deepening until 1800 UTC.

376 Observed surface wind speeds near the Wasatch Front at 1200 UTC and 2100 UTC are
377 superimposed on the surface wind fields simulated by the model in Fig. 13. The simulated
378 winds are comparable to those observed near the base of the lee slopes of the Wasatch
379 Mountains at 1200 UTC, including the localized maximum near Centerville. By later in the
380 day (2100 UTC), the model has shifted the strongest winds farther north, but the simulated
381 winds appear too strong compared to observations. The winds along the crest in the model
382 are lower than those observed; for example, simulated wind speeds were $10\text{--}15\text{ m s}^{-1}$, while
383 the winds observed at OGP and other crest-level stations at Snowbasin Ski Resort (not

384 shown) were greater than 20 m s^{-1} (see also Fig. 8c). As will be shown in greater detail
385 later, the model tends to accelerate the flow down the slopes of the Wasatch Mountains
386 more strongly than is likely taking place. The WRF model develops rotors and trapped
387 waves, and these phenomena appear in the valley surface winds at 2100 UTC as bands of
388 increased and decreased winds in bands oriented parallel to the upstream terrain. In this
389 1.3-km domain simulation, strong winds do not extend out over the Great Salt Lake, whereas
390 operational NWS 4-km WRF model forecasts (not shown) suggested a westward extension
391 of $25\text{--}30 \text{ m s}^{-1}$ gusts as far west as Antelope Island (labelled AI in Fig. 13).

392 The time evolution of wind speed and direction during the simulated downslope wind-
393 storm is now related in Fig. 14 to that observed at Glover's Lane (UFD04) (previously shown
394 in Fig. 8b). The Control simulation shows remarkable agreement with the observations re-
395 garding the timing and general evolution of the intensity of the surface winds. However, the
396 simulated windstorm continues for ~ 2 h longer than that observed.

397 Figure 9 compares the vertical profiles of temperature, moisture, and wind at KSLC at
398 1200 UTC from the Control simulation to the observed sounding. The model captures the
399 basic vertical structure, but the simulated vertical profiles differ from those observed in sev-
400 eral key respects: (1) surface westerly return flow rather than decoupled down-valley winds;
401 (2) peak easterly flow near the base of a stable layer at 775 hPa relative to that observed
402 near 700 hPa; (3) deep well-mixed layer between 750–550 hPa with near-zero cross-barrier
403 flow at 600 hPa, and more stable conditions and weak cross-barrier flow above ~ 475 hPa;
404 and (4) generally lower dewpoint temperature throughout the troposphere.

405 To further evaluate the control simulation, we now present cross-sections of potential
406 temperature and horizontal wind from the control simulation. The first cross-section lies
407 along the southwest–northeast (A–B) transect shown in Fig. 1, starting from the Great Salt
408 Lake, through Centerville and terminating near Lyman, WY (Fig. 15). The wind components
409 from the WRF model are rotated 20° counterclockwise to create plane-parallel winds at all
410 levels. Note that the terrain height is lower in the model than that observed: as a result of

411 smoothing, the model's Wasatch Range is \sim 250 m lower than the actual terrain.

412 In the top panel of Fig. 15, at 1200 UTC, 20 m s^{-1} flow from the northeast (right to left
413 in the figure) approaches the Wasatch Front, and then plunges sharply into the valley as a
414 downslope windstorm. Note how the colder air (lower potential temperature) pools in the
415 upstream valley, effectively creating an unobstructed horizontal pathway for the low-level
416 easterly jet. Downstream of the Wasatch crest, strong winds continue for more than 10 km
417 along the valley floor before forming a rotor. Under this first rotor, $5\text{--}10 \text{ m s}^{-1}$ westerly
418 winds oppose the windstorm easterlies. The area of strong surface winds is broader than
419 observed, i.e., observations suggest the rotor clouds and return flow begin roughly 10 km
420 from the crest, while the model shifts that farther west. In the bottom panel, at 2100 UTC,
421 the upstream stable layer has intensified as a result of both terrestrial heating and continued
422 cold advection in the planetary boundary layer at \sim 3000 m. This enhances the formation
423 of mountain waves above the upstream terrain. The formation of rotors at this time occurs
424 closer to the crest, though it is important to note that these images are merely snapshots;
425 the locations of the non-linear internal gravity waves shift with time as a result of dynamical
426 and turbulent processes (e.g., Hertenstein 2009).

427 As evident in the Skew-T diagram for KSLC (Fig. 9), the model's strongest easterly winds
428 tend to be at a lower height over the terrain than observed. This may explain the model's
429 tendency to confine flow to follow the terrain slope more closely than observed, i.e., the
430 elevated flow extending westward away from the crest is missing from the model. Note also
431 that the simulated winds immediately above the Wasatch crest are weak (see also Fig. 13),
432 which contributes to flow descending at a steeper angle associated with the lee waves. The
433 model also does not capture the strong capping inversion above the rotor observed near
434 Centerville.

435 Cross-sections of vertical motion indicate ascent within the rotor at 1200 UTC is on the
436 order of $20\text{--}30 \text{ m s}^{-1}$ (not shown), which is broadly consistent with the ascent rate estimated
437 from the Centerville rawinsonde at this time. However, the overall structure of the simulated

438 downslope windstorm is too intense, relative to that inferred from the Centerville sounding
439 and other observational evidence. The strong subsidence, 2-km plunging of the isentropes,
440 and extreme drying in the lee of the mountains is not likely to have taken place during
441 this event. The lee waves continue to amplify through the time of the later cross-section as
442 evident by the isentropes in Fig. 15 at 2100 UTC.

443 Cross-sections perpendicular to the upstream flow (i.e., roughly north–south across a
444 swath of lower terrain in Wyoming and extending into the Uinta mountains; C–D in Fig. 1)
445 are generated by rotating the wind components $\sim 5^\circ$ counterclockwise (Fig. 16). At 1200 UTC,
446 the simulation generates a barrier-jet-like core of $15\text{--}20 \text{ m s}^{-1}$ easterly winds to the north of
447 the Uinta mountains. By 2100 UTC, the strong easterly flow has extended farther north, as
448 the cut-off low reaches a position directly south of the Wasatch Front. These factors may
449 help to explain the observed northward progression of strong winds along the Wasatch Front
450 as a result of the more windstorm-favorable easterlies extending farther north later in the
451 day.

452 *d. Sensitivity to Uinta Mountains*

453 The Uinta Mountains are a substantial barrier and have the distinction of being the
454 highest mountain range (a crest line above 3000 m) in the contiguous United States oriented
455 in the east–west direction. Their location south of the open expanses of western Wyoming
456 may contribute to channeling easterly winds towards the Wasatch Mountains. To test the
457 sensitivity of the windstorm’s strength and occurrence to the upstream terrain, we now
458 present results of a modeling experiment (referred to as the No-Uinta simulation) in which
459 the Uinta Mountains are flattened. Following similar WRF-terrain modifications by West
460 and Steenburgh (2011) and Alcott and Steenburgh (2013), the impact of the Uinta Mountains
461 on the 1 December 2011 Wasatch downslope windstorm is investigated by completing a
462 simulation in which the terrain height of the Uintas above 2300 m is lowered to that elevation
463 on the 4- and 1.3-km domains (the Uintas remain unchanged on the 12-km domain to

464 minimize discontinuities on the largest scales). This has two additional impacts: (1) the
465 resultant void is replaced by a volume of standard-atmosphere air, and (2) soil temperatures
466 are replaced with the deep-soil values in places where the upper soil layers have been removed.
467 Due to the strong dynamical forcing of this event, these two changes are unlikely to greatly
468 affect the simulation in comparison to the changes arising from the altered terrain. The use
469 of two-way feedback between the nested domains implies that the Uintas' presence in the
470 outer domain may still be felt to some extent on the inner domains, i.e., the impact of their
471 removal may be underestimated here.

472 Figure 17 shows the zonal wind difference (No-Uinta minus Control) after reducing the
473 height of the Uinta mountains. At 1200 UTC, there is a strong increase–decrease dipole
474 centered near Salt Lake City (marked by SLC). North of Salt Lake City, easterly winds
475 have been markedly reduced by the removal of the Uinta Mountains (elevations of which are
476 contoured in red). The decreased easterly flow north of the Uinta mountains' former position
477 supports the hypothesis that the Uintas obstruct southward flow and create a barrier jet
478 towards the northern Wasatch Front. Conversely, easterly winds have strengthened to the
479 south of Salt Lake City, particularly around the city of Provo in the southern Wasatch Front.
480 Without the Uintas, the northeasterly flow from Wyoming is unimpeded and plunges over
481 the Wasatch farther south as a downslope windstorm in that region.

482 Later at 2100 UTC—with or without the Uinta mountains—there are strong easterly
483 winds in the northern Wasatch Front, confirming the importance of the orientation of large-
484 scale midtropospheric winds; i.e., when the large-scale flow becomes more easterly, the impact
485 of the blocking by the Uintas is lessened. The reduced elevation of the Uintas allows the
486 windstorm to continue in the southern Wasatch Front at this time. Overall, an increased east-
487 erly component appears to initiate mountain waves more easily along the northern Wasatch
488 Front. In contrast, the presence of the Uintas likely shields the southern Wasatch Front from
489 damaging winds on many occasions. The time series of simulated surface wind at UFD04,
490 with (green) and without (red) the Uintas, are shown in Fig. 14, and corroborates the sen-

491 sensitivity of valley wind speed to the orientation of the large-scale flow. Without the Uintas,
492 the downslope easterly flow is weaker until the model's synoptic-scale flow becomes more
493 easterly after 1500 UTC.

494 Cross-sections are now shown as before, but with the Uinta mountains reduced in elevation
495 (Figs. 18 and 19). While the stability is comparable, a weaker jet crosses the Wasatch
496 crest at 1200 UTC (Fig. 18). This results in weaker mountain waves, which do not penetrate
497 to the floor of the Wasatch Front. At 2100 UTC, wind speeds are still slightly weaker than
498 the Control run, though strong winds now reach the valley floor. A comparison of vertical
499 wind speeds from the No-Uinta and Control simulations indicates the weaker mountain
500 wave pattern downstream of the Wasatch crest at both times in the No-Uinta simulation
501 (not shown). The north-south No-Uinta cross-section (Fig. 19) maintains a core of strong
502 easterlies at 1200 UTC from the control run, though this core is more elongated than the
503 Control.

504 4. Summary

505 This study documented the severe downslope windstorm in northern Utah on 1 December
506 2011, which caused over \$75m damage along the Wasatch Front. This event had the second-
507 highest maximum wind speed and gust recorded at KHIF since 1979. A brief climatological
508 analysis of earlier events highlighted the lack of downslope windstorms in this area in the
509 period 2000–2010. Identifying the causes for this temporal gap has been inconclusive. There
510 was no strong evidence to suggest that crest-level easterly winds were simply less frequent
511 during the 2000–2010 period (Fig. 4) nor that ARWB events were less frequent.

512 The 1 December 2011 downslope windstorm occurred as a result of a well-defined synoptic
513 setting, which can be summarized as follows:

- 514 • An ARWB event over western North America established the prevailing easterly flow in
515 the midtroposphere over the Wasatch Mountains. The stalling of the associated mid-

516 tropospheric cut-off low over southern Nevada maintained this easterly flow's position
517 over the Wasatch range, and sustained the downslope windstorm past their typical
518 demise during late morning.

- 519 • The gradient easterly wind near crest-level (700 hPa) developed rapidly between 0600
520 and 1200 UTC, initially oriented from the northeast, but veering by 1800 UTC to be
521 more directly from the east before weakening after 2100 UTC.
- 522 • Common to downslope windstorms in other areas, mountain waves generated from the
523 easterly flow orthogonal to the Wasatch may have been reflected back towards the
524 surface by the stable layer (Smith 1985). This process may have also generated its own
525 critical layer, seen in observational and numerical-simulation data, where the cross-
526 barrier component to the flow falls to zero (Peltier and Clark 1979) in downstream,
527 and not upstream, profiles.
- 528 • As the large-scale lower-tropospheric height gradient from Wyoming to Nevada in-
529 creased during the day, cold air surged across Wyoming. The Uinta Mountains may
530 have shunted initial northeasterly flow towards the Wasatch Front, leading to a barrier-
531 jet-like feature associated with strong cold advection. Cold air filled in the lowest de-
532 pressions allowing the barrier jet to continue downstream (and immediately upstream
533 of the Wasatch Mountains at Morgan, UT) at an elevation of a few hundred meters
534 above crest level.

535 The localized nature of Wasatch downslope windstorms was readily apparent during this
536 event. The downslope winds began abruptly at \sim 0900 UTC resulting from the initial push
537 of the easterly flow across the Wasatch Mountains and trapped beneath the stable layer
538 farther aloft. The strongest winds were observed at \sim 1500 UTC in Centerville, and ended
539 abruptly in that area after 1900 UTC. A feature of this event uncommon to previous ones
540 was the progression through midday of the strongest winds, and the subsequent damage
541 farther north. The cross-barrier flow measured at OGP immediately above the locations

542 in Weber County where damage occurred (including the Weber State University campus)
543 continued to increase until late afternoon as a result of the synoptic-scale shifts in the large-
544 scale flow. Observations during the morning from a vehicle-mounted sensor filled the spatial
545 gaps between the automated observing sites along the Wasatch Front. Although peak winds
546 were observed at numerous favored locations (fewer upstream obstructions, etc.), there was
547 a general uniformity of the flow spilling over the mountains and reaching their base (i.e.,
548 widespread strong easterly winds of quasi-constant potential temperature that was close
549 to values observed at jet level upstream of the Wasatch, and low dewpoint temperature).
550 Lower temperatures within Weber River Canyon, sampled by the vehicle-mounted sensor
551 and nearby stations, indicated the additional effects of low-level gap flows travelling through
552 this canyon.

553 The data from the rawinsonde released at 1100 UTC in Centerville revealed a clear un-
554 derflow near the surface (Armi and Mayr 2011) before the sonde ascended rapidly within a
555 rotor. A sharp subsidence inversion capped the rotor with strong winds observed at that
556 level. This bifurcation of the strongest winds (at the surface and at the level of the inversion)
557 is similar to that found in large-eddy simulations of downslope flows (e.g., Hertenstein 2009).
558 The characteristics of a self-induced critical layer farther aloft may also be evident (Peltier
559 and Clark 1979). The localized nature of the characteristic features of downslope windstorms
560 below the crest of the Wasatch Range found near Centerville is apparent by comparing the
561 vertical profiles at Centerville to the sounding at KSLC. The KSLC sounding has typical
562 morning downvalley flows, decoupled from a well-mixed layer below crest-level, and hints of
563 strong turbulence below a strong inversion near 700 hPa. Not surprisingly, the two profiles
564 of temperature, moisture, and wind are quite similar to one another above crest level.

565 Even with the relatively-rich observational dataset available to examine this windstorm,
566 a high-resolution WRF numerical simulation forced by NAM-analyzed conditions on the
567 outer boundary provides critical information on the dynamical and thermodynamical struc-
568 ture associated with the event. The WRF simulation captured many of the synoptic-scale

569 features evident from the ERA-Interim Reanalyses. However, the breaking of the Rossby
570 wave in the Control simulation was slightly slower; deepening of the cut-off low in the model
571 simulation continued until 1800 UTC over southern Nevada, whereas at this point, ERA-
572 Interim reanalysis showed filling of the low to have already started. The model 10-m winds
573 along the Wasatch Front had many similarities to those observed, including the location of
574 the maximum winds. However, the model's 10-m winds at crest level tended to be weaker
575 than those observed along the crest. The model's response to the flow across the Wasatch
576 barrier beneath the strong stable layer is to develop mountain waves larger in amplitude
577 than was likely present. This results in model vertical profiles at the western base of the
578 Wasatch Mountains that are more akin to extreme-amplitude mountain-wave windstorms
579 (e.g., Grubišić and Billings 2008). The model creates a band of dry air, flowing parallel
580 down the terrain along isentropes, from high above the model terrain and plunging close to
581 the surface. A lateral jet, evident in the Centerville observed profile near crest level, does
582 not form in the model simulations.

583 Following similar WRF-terrain modifications by West and Steenburgh (2011) and Alcott
584 and Steenburgh (2013), we investigated whether the Uinta Mountains (a major barrier to
585 meridional flow across the Wyoming–Utah border) steer northeasterly lower-tropospheric
586 flow more directly towards the Wasatch Mountains, potentially supporting windstorms in
587 Davis County earlier in the synoptic pattern progression. If the Uinta Mountains in the WRF
588 model are reduced in elevation comparable to that found over much of western Wyoming,
589 then southwestward cold advection spills farther south across the Wasatch Front in the
590 absence of the blocking terrain. However, as the synoptic-scale flow later in the day veers
591 towards a more easterly direction, then the blocking effect of the Uinta Mountains is lessened.

592 The NWS first mentioned a possible downslope windstorm along the Wasatch Front \sim 90 h
593 before its onset. Confidence in this forecast was supported by operational deterministic
594 high-resolution model runs. In contrast, Reinecke and Durran (2009) evaluated ensemble
595 forecasts of downslope windstorms in the lee of the Sierra Mountains of California and

596 estimated predictability timescales of $O(12\text{ h})$ for their two case studies. As summarized by
597 Doyle et al. (2013), numerous studies have suggested that error growth might be reduced,
598 and predictability enhanced, for mesoscale phenomena such as downslope windstorms as
599 a result of terrain-flow interactions. Furthermore, events that are strongly coupled with
600 larger-scale (i.e., typically more-predictable) phenomena such as ARWB events may inherit
601 some predictability tendency from the larger scales, which may help (Palmer 1993) or hinder
602 (Durran and Gingrich 2014) smaller-scale forecasts. We will attempt in a separate study
603 to understand the apparent enhanced predictability for this downslope windstorm event
604 using 11-member ensembles from the Global Ensemble Forecast System Reforecast, Version
605 2 (Hamill et al. 2013), using ensemble reforecasts starting as early as 25 November 2011
606 (150 h before the onset of the strong winds).

607 *Acknowledgments.*

608 We thank Professors Courteney Strong and Jim Steenburgh for useful suggestions; Erik
609 Crosman and Trevor Alcott for much valuable advice; Roger Akers, Chris Ander, Erik Cros-
610 man, Alex Jacques, Matt Lammers, Nola Lucke, Wil Mace, and Trevor Alcott, all for assis-
611 tance in collecting data during the windstorm; the Center for High-Performance Computing
612 at the University of Utah for provision of, maintenance of, and assistance with the super-
613 computers. This research was supported by NOAA/NWS Collaborative Science, Technology,
614 and Applied Research Program Grant NA10NWS4680005.

REFERENCES

- 617 Alcott, T. and W. J. Steenburgh, 2013: Orographic influences on a Great Salt Lake-effect
 618 snowstorm. *Mon. Wea. Rev.*, **141**, 2432–2450.
- 619 Armi, L. and G. J. Mayr, 2011: The descending stratified flow and internal hydraulic jump
 620 in the lee of the Sierras. *J. Appl. Meteor. Climatol.*, **50**, 1995–2011.
- 621 Chrust, M. F., C. D. Whiteman, and S. W. Hoch, 2013: Observations of thermally driven
 622 wind jets at the exit of Weber Canyon, Utah. *J. Appl. Meteor. Climatol.*, **52**, 1187–1200.
- 623 Dee, D. P., S. M. Uppala, A. J. Simmons, P. Berrisford, P. Poli, S. Kobayashi, U. Andrae,
 624 M. A. Balmaseda, G. Balsamo, P. Bauer, P. Bechtold, A. C. M. Beljaars, L. van de Berg,
 625 J. Bidlot, N. Bormann, C. Delsol, R. Dragani, M. Fuentes, A. J. Geer, L. Haimberger,
 626 S. B. Healy, H. Hersbach, E. V. Hólm, L. Isaksen, P. Kållberg, M. Köhler, M. Matricardi,
 627 A. P. McNally, B. M. Monge-Sanz, J.-J. Morcrette, B.-K. Park, C. Peubey, P. de Rosnay,
 628 C. Tavolato, J.-N. Thépaut, and F. Vitart, 2011: The ERA-Interim reanalysis: configu-
 629 ration and performance of the data assimilation system. *Q. J. Roy. Meteor. Soc.*, **137**,
 630 553–597.
- 631 Doyle, J. and D. Durran, 2002: The dynamics of mountain-wave-induced rotors. *J. Atmos.
 632 Sci.*, **59**, 186–201.
- 633 Doyle, J., C. Epifanio, A. Persson, P. Reinecke, and G. Zängl, 2013: Mesoscale modeling over
 634 complex terrain: numerical and predictability perspectives. *Mountain Weather Research
 635 and Forecasting: Recent Progress and Current Challenges*, F. Chow, S. De Wekker, and
 636 B. Snyder, eds., Springer, 531–590.
- 637 Durran, D. R. and M. Gingrich, 2014: Atmospheric predictability: Why butterflies are not
 638 of practical importance. *J. Atmos. Sci.*, in press.

- 639 Grubišić, V. and B. J. Billings, 2008: Climatology of the Sierra Nevada mountain-wave
640 events. *Mon. Wea. Rev.*, **136**, 757–768.
- 641 Hamill, T. M., G. T. Bates, J. S. Whitaker, D. R. Murray, M. Fiorino, T. J. Galarneau,
642 Y. Zhu, and W. Lapenta, 2013: NOAA’s second-generation global medium-range ensemble
643 reforecast data set. *Bull. Am. Meteorol. Soc.*, **94**, 1553–1565.
- 644 Hertenstein, R. F., 2009: The influence of inversions on rotors. *Mon. Wea. Rev.*, **137**, 433–
645 446.
- 646 Holland, L., 2002: *Downslope windstorms along the Wasatch Front*. M.S. Thesis, University
647 of Utah, 86 pp.
- 648 Horel, J., T. Potter, L. Dunn, W. Steenburgh, M. Eubank, M. Splitt, and D. Onton, 2002a:
649 Weather support for the 2002 Winter Olympic and Paralympic Games. *Bull. Amer. Me-*
650 *teor. Soc.*, **83**, 227–240.
- 651 Horel, J., M. Splitt, L. Dunn, J. Pechmann, B. White, C. Ciliberti, S. Lazarus, J. Slemmer,
652 D. Zaff, and J. Burks, 2002b: Mesowest: cooperative mesonet in the western United
653 States. *Bull. Amer. Meteor. Soc.*, **83**, 211–225.
- 654 Jiang, Q. and J. D. Doyle, 2008: Diurnal Variation of Downslope Winds in Owens Valley
655 during the Sierra Rotor Experiment. *Mon. Wea. Rev.*, **136**, 3760–3780.
- 656 Jones, C., J. Colton, R. McAnelly, and M. Meyers, 2002: An examination of a severe downs-
657 lope windstorm west of the Colorado Park Range. *Natl. Weather Dig.*, **26**, 73–81.
- 658 Kühnlein, C., A. Dörnbrack, and M. Weissmann, 2013: High-Resolution doppler lidar ob-
659 servations of transient downslope flows and rotors. *Mon. Wea. Rev.*, **141**, 3257–3272.
- 660 Lareau, N. P., E. Crosman, C. D. Whiteman, J. Horel, S. W. Hoch, W. O. J. Brown, and
661 T. W. Horst, 2013: The Persistent Cold-Air Pool Study. *Bull. Amer. Meteor. Soc.*, **94**,
662 51–63.

- 663 Lawson, J., 2013: *Analysis and predictability of the 1 December Wasatch downslope wind-*
664 *storm*. M.S. Thesis, University of Utah, 84 pp.
- 665 Lilly, D. K. and E. J. Zipser, 1972: The front range windstorm of 11 january 1972: a
666 meteorological narrative. *Weatherwise*, **25**, 56–63.
- 667 Markowski, P. and Y. Richardson, 2010: *Mesoscale Meteorology in Mid-latitudes*. Wiley-
668 Blackwell, 407 pp.
- 669 Mass, C. and M. Albright, 1985: A severe windstorm in the lee of the cascade mountains of
670 washington state. *Mon. Weather Rev.*, **113**, 1261–1281.
- 671 Miller, P. and D. Durran, 1991: On the sensitivity of downslope windstorms to the asym-
672 metry of the mountain profile. *J. Atmos. Sci.*, **48**, 1457–1473.
- 673 O'Donoghue, A. J., 2012: Remembering the winds of 2011: Utah's 'most devastating wind
674 event' in decades happened 1 year ago. *Deseret News*, Salt Lake City.
- 675 Palmer, T., 1993: Extended-range atmospheric prediction and the Lorenz model. *Bull. Amer.*
676 *Meteor. Soc.*, **74**, 49–65.
- 677 Peltier, W. and T. Clark, 1979: The evolution and stability of finite-amplitude mountain
678 Waves. Part II: surface wave drag and severe downslope windstorms. *J. Atmos. Sci.*, **36**,
679 1498–1529.
- 680 Reinecke, P. and D. Durran, 2009: Initial-condition sensitivities and the predictability of
681 downslope winds. *J. Atmos. Sci.*, **66**, 3401–3418.
- 682 Richner, H. and P. Hächler, 2013: Understanding and forecasting Alpine Foehn. *Mountain*
683 *Weather Research and Forecasting: Recent Progress and Current Challenges*, F. Chow,
684 S. De Wekker, and B. Snyder, eds., Springer, 219–260.
- 685 Smith, R., 1985: On severe downslope winds. *J. Atmos. Sci.*, **42**, 2597–2603.

- 686 Strong, C. and G. Magnusdottir, 2008: Tropospheric Rossby wave breaking and the
687 NAO/NAM. *J. Atmos. Sci.*, **65**, 2861–2876.
- 688 Thorncroft, C. D., B. Hoskins, and M. McIntyre, 1993: Two paradigms of baroclinic-wave
689 life-cycle behaviour. *Q. J. Roy. Meteor. Soc.*, **119**, 17–55.
- 690 Vosper, S., 2004: Inversion effects on mountain lee waves. *Q. J. Roy. Meteor. Soc.*, **130**,
691 1723–1748.
- 692 Wang, T.-A. and Y.-L. Lin, 1999: Wave ducting in a stratified shear flow over a Two-
693 Dimensional mountain. part II: Implications for the development of High-Drag states for
694 severe downslope windstorms. *J. Atmos. Sci.*, **56**, 437–452.
- 695 Welch, W. and D. Rice, 2011: 100-mph Santa Ana winds whip Southwest. *USA Today*.
- 696 West, G. L. and W. Steenburgh, 2011: Influences of the Sierra Nevada on Intermountain
697 cold-front evolution. *Mon. Wea. Rev.*, **139**, 3184–3207.
- 698 Whiteman, C. D., 2000: *Mountain Meteorology: Fundamentals and Applications*. Oxford
699 University Press, USA, New York, 355 pp.
- 700 Zhong, S., J. Li, C. David Whiteman, X. Bian, and W. Yao, 2008: Climatology of high wind
701 events in the owens valley, california. *Mon. Weather Rev.*, **136**, 3536–3552.

₇₀₂ **List of Tables**

₇₀₃ 1	Parameterization schemes used in numerical modeling configuration.	30
₇₀₄ 2	Downslope windstorm events at KHIF as defined by this study.	31

Table 1: Parameterization schemes used in numerical modeling configuration.

Parameterization	Scheme
Microphysics	WRF Single-Moment 3-class Scheme
Longwave Radiation	RRTM Scheme
Shortwave Radiation	Dudhia Scheme
Surface Layer	MM5 Similarity
Land Surface	Noah Land Surface Model (with snow effect)
Urban Surface	Switched off
Planetary Boundary Layer	Yonsei University Scheme
Cumulus Parameterization	Kain-Fritsch Scheme (12-km, 4-km domains only)
Latent/Sensible Heat Flux	Allowed
Vertical Velocity Damping	Switched off
6th Order Horizontal Diffusion	Simple (12-km domain only)

Table 2: Downslope windstorm events at KHIF as defined by this study.

Date	Time of max. wind, UTC	Max. wind speed m s^{-1} (mph)	Max. wind gust m s^{-1} (mph)
9 October 1979	1500	15 (34)	21 (48)
19 January 1980	1200	15 (34)	22 (49)
4 April 1983	1700	21 (46)	31 (70)
30 March 1984	1200	15 (34)	18 (41)
16 January 1987	1740	15 (34)	20 (44)
24 December 1987	0700	15 (34)	21 (46)
15 December 1988	1200	16 (36)	23 (51)
30 January 1993	1700	18 (41)	21 (48)
12 January 1997	1100	17 (38)	23 (52)
24 February 1997	1700	18 (40)	23 (51)
2 April 1997	1600	15 (34)	24 (53)
23 April 1999	1755	18 (40)	24 (53)
1 December 2011	1655	20 (45)	30 (67)

705 **List of Figures**

- 706 1 Terrain elevation and locations in northern Utah and western Wyoming (shad-
707 ing). (a) Locations (Salt Lake International Airport, KSLC; and Hill Air Force
708 Base, KHIF), mountain ranges, and cross-section paths mentioned in the text
709 are shown. The shaded rectangular box along the Wasatch Front approx-
710 imately delineates the damage swatch on 1 December 2011. The Wasatch
711 Front is the low-lying region paralleling the west slopes of the Wasatch Moun-
712 tains. (b) Zoomed-in view with locations discussed in the text. 36
- 713 2 Anemometers installed in Centerville, UT, by Union Pacific Railroad (MesoWest
714 identifier: CENWWS; foreground) and Utah Department of Transportation
715 (MesoWest identifier: CEN; background), at the location of strongest observed
716 winds during the 1 December 2011 windstorm. 37
- 717 3 Domain areas for the 12-, 4-, and 1.3-km domains in the Weather Research
718 and Forecasting model. Terrain is from the 12-km domain at 10-min resolution. 38
- 719 4 Sustained wind (shaded bars) associated with downslope windstorms as a
720 function of winter season at KHIF according to the scale on left. Filled circles
721 indicate the maximum gust associated with each windstorm. Percent of season
722 with strong 700 hPa winds from easterly direction in ERA-Interim Reanalysis
723 data marked by black line according to scale on the right. Two (three) events
724 occur in the winter of 1979/80 (1996/97) and hence overlap on the chart. 39
- 725 5 Evolution of ERA-Interim 700-hPa geopotential height (contoured at 30-m
726 intervals), composited over 13 downslope windstorm events at (a) 0000 UTC,
727 (b) 0600 UTC, (c) 1200 UTC, and (d) 1800 UTC 40
- 728 6 Evolution of 700-hPa geopotential height (contoured at 30-m intervals) and
729 wind speed (shading according to scale) on 1 December 2011, taken from the
730 ERA-Interim dataset, at (a) 0000 UTC, (b) 0600 UTC, (c) 1200 UTC, and
731 (d) 1800 UTC.. 41

- 732 7 Mobile wind observations from 0915–1015 UTC. Vector arrows are relative to
 733 scale in top-left. Distance is according to the scale in bottom-left. Filled
 734 contours indicate terrain, taken from innermost WRF domain, with scale at
 735 bottom. Observation stations mentioned in text are labelled. 42
- 736 8 Surface wind observations at (a) Hill Air Force Base (KHIF), (b) Glover's
 737 Lane (UFD04), and (c) Ogden Peak (OGP) on 1 December 2011. Wind
 738 speed, wind gust, and wind direction shown by solid lines, filled circles, and
 739 crosses, respectively. All available KHIF observations are shown; for clarity,
 740 UFD04 and OGP data are sampled at 30-min intervals from the data available
 741 at higher reporting intervals. 43
- 742 9 Skew-T log-P profiles at 1200 UTC 1 December 2011, from observed rawin-
 743 sonde launch at KSLC (black lines) and from the WRF Control simulation
 744 at the nearest grid point (blue lines). Temperature, dew-point temperature,
 745 and wind denoted by solid lines, dashed lines, and barbs (full barb 5 m s^{-1}),
 746 respectively. For clarity, wind barbs from only selected model levels are shown. 44
- 747 10 Vertical profiles of observed rawinsonde data near Morgan, UT, and Center-
 748 ville, UT (near CENWWS). (a) Potential temperature (solid line), relative
 749 humidity (dashed line), wind speed (crosses), and wind direction (open cir-
 750 cles) at Morgan, UT, at 1800 UTC 1 December 2011, as a function of height.
 751 (b) As in (a) but for the 1200 UTC Centerville, UT launch. 45
- 752 11 Comparison of rawinsonde ascent rates (m s^{-1}) at Morgan, UT (1800 UTC;
 753 crosses) and Centerville (1200 UTC; open circles). 46
- 754 12 WRF Control simulation 700-hPa geopotential height fields (contoured at 30-
 755 m interval), at (a) 0000 UTC, (b) 0600 UTC, (c) 1200 UTC, and (d) 1800
 756 UTC, all 1 December 2011. Noisy contours result from the 700-hPa surface
 757 intersecting the model terrain. 47

- 758 13 Comparison of observed surface wind speeds (colored circles) versus Control-
759 simulation surface wind speeds (shading), both according to scale at bottom.
760 The wind measurements are taken from the observation time closest to (a)
761 1200 UTC and (b) 2100 UTC, within 30 min either side of the respective times,
762 for each available station. WRF innermost-domain terrain contoured every
763 400 m for reference; Antelope Island marked with “AI”. 48
- 764 14 Observed and simulated surface winds at Glover’s Lane (UFD04), UT on 1
765 December 2011. Observed wind speeds and wind directions from UFD04 are
766 denoted by black solid lines and filled circles, respectively. Simulated surface
767 wind speeds and directions from the Control (No-Uinta) simulations are shown
768 by the green (red) solid lines and filled circles, respectively. Wind direction
769 data from all three sources have been subsampled to every 20 minutes for clarity. 49
- 770 15 Perpendicular-to-Wasatch cross-section from innermost WRF domain (A–B in
771 Fig. 1) at (a) 1200 UTC and (b) 2100 UTC, 1 December 2011. Shading denotes
772 plane-parallel wind component according to the scale (e.g., blue indicates flow
773 from right to left), while potential temperature is contoured at an interval of
774 2 K. 50
- 775 16 Roughly north–south cross-section from innermost WRF domain (C–D in
776 Fig. 1) through west-central Wyoming (left) to the southern slopes of the
777 Uintas (right) at (a) 1200 UTC and (b) 2100 UTC, 1 December 2011. Shad-
778 ing denotes wind component in and out of the page (e.g., blue indicates pre-
779 dominantly easterly flow out of the page) according to the scale; potential
780 temperature is contoured at an interval of 2 K. 51

- 781 17 Zonal wind difference (No-Uinta minus Control), shaded according to the scale
782 at the bottom, at (a) 1200 UTC and (b) 2100 UTC, 1 December 2011. Black
783 (red) contours at 500-m intervals denote the elevation of the terrain used
784 in both the Control and No-Uinta (Control only) simulations. Blue (red)
785 indicates an increase (decrease) in easterly wind in this location as a result of
786 removing the Uinta mountains. 52
- 787 18 As in Fig. 15, but from the no-Uinta WRF simulation. 53
- 788 19 As in Fig. 16, but from the no-Uinta WRF simulation. 54

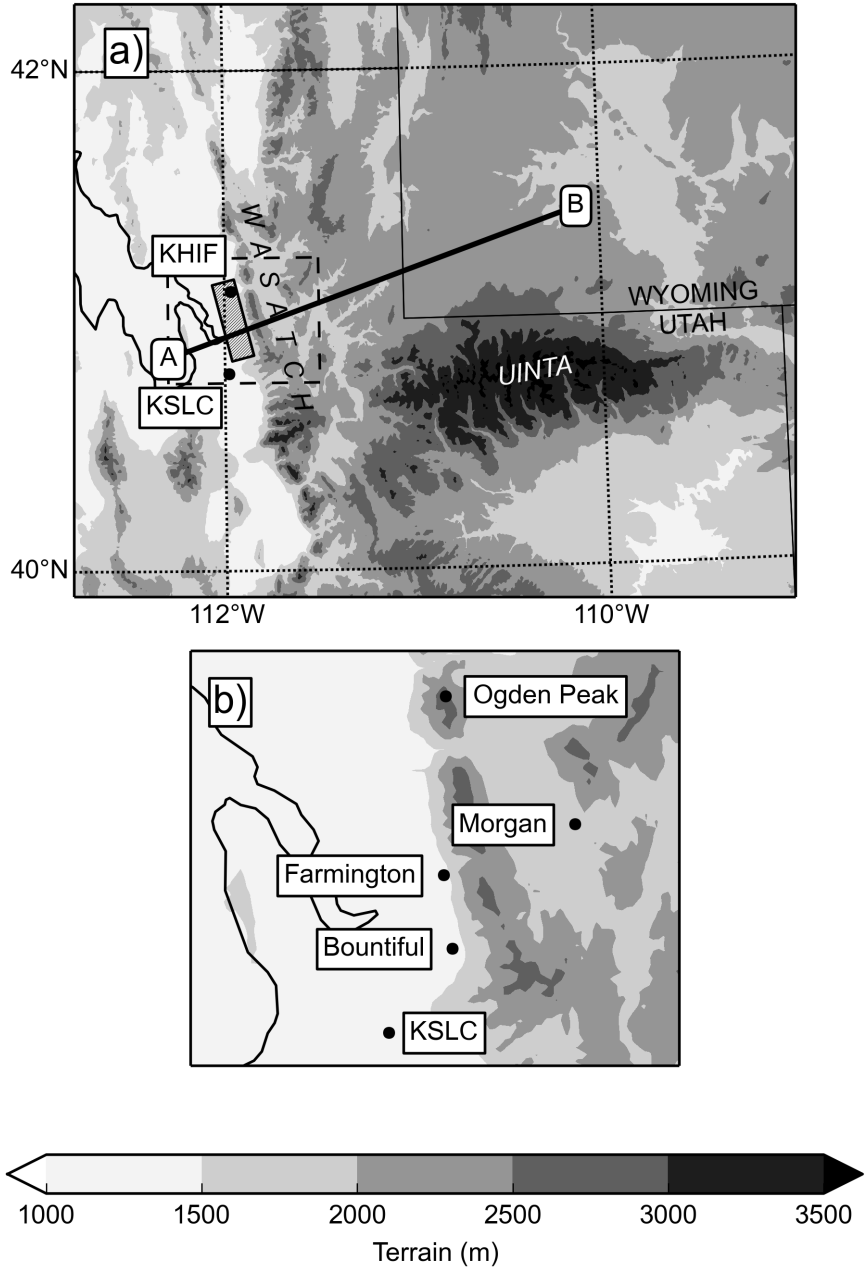


Figure 1: Terrain elevation and locations in northern Utah and western Wyoming (shading). (a) Locations (Salt Lake International Airport, KSLC; and Hill Air Force Base, KHIF), mountain ranges, and cross-section paths mentioned in the text are shown. The shaded rectangular box along the Wasatch Front approximately delineates the damage swatch on 1 December 2011. The Wasatch Front is the low-lying region paralleling the west slopes of the Wasatch Mountains. (b) Zoomed-in view with locations discussed in the text.



Figure 2: Anemometers installed in Centerville, UT, by Union Pacific Railroad (MesoWest identifier: CENWWS; foreground) and Utah Department of Transportation (MesoWest identifier: CEN; background), at the location of strongest observed winds during the 1 December 2011 windstorm.

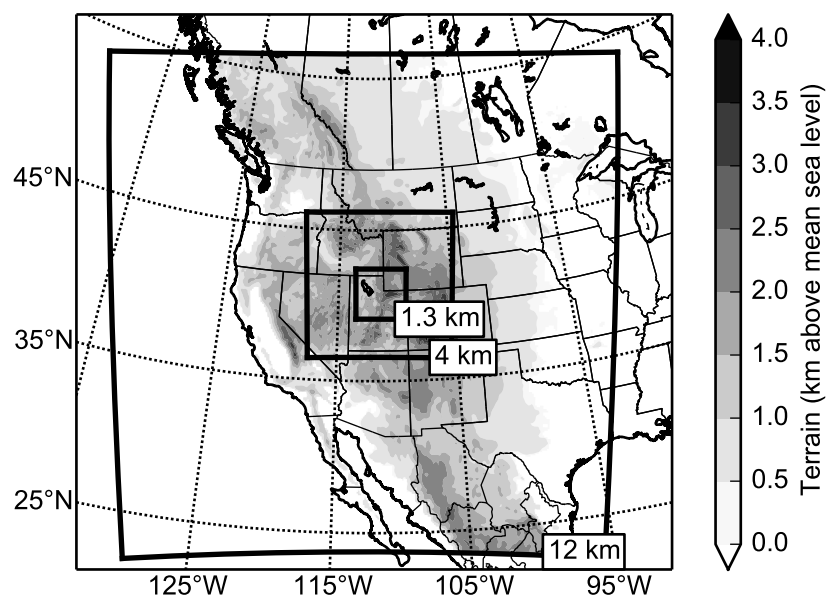


Figure 3: Domain areas for the 12-, 4-, and 1.3-km domains in the Weather Research and Forecasting model. Terrain is from the 12-km domain at 10-min resolution.

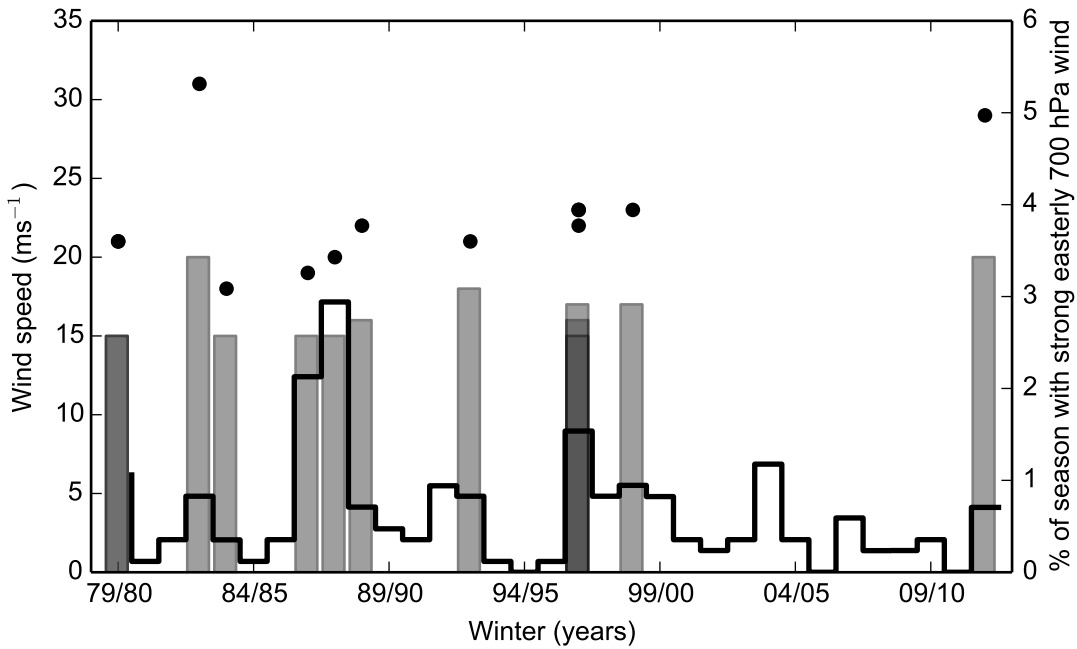


Figure 4: Sustained wind (shaded bars) associated with downslope windstorms as a function of winter season at KHIF according to the scale on left. Filled circles indicate the maximum gust associated with each windstorm. Percent of season with strong 700 hPa winds from easterly direction in ERA-Interim Reanalysis data marked by black line according to scale on the right. Two (three) events occur in the winter of 1979/80 (1996/97) and hence overlap on the chart.

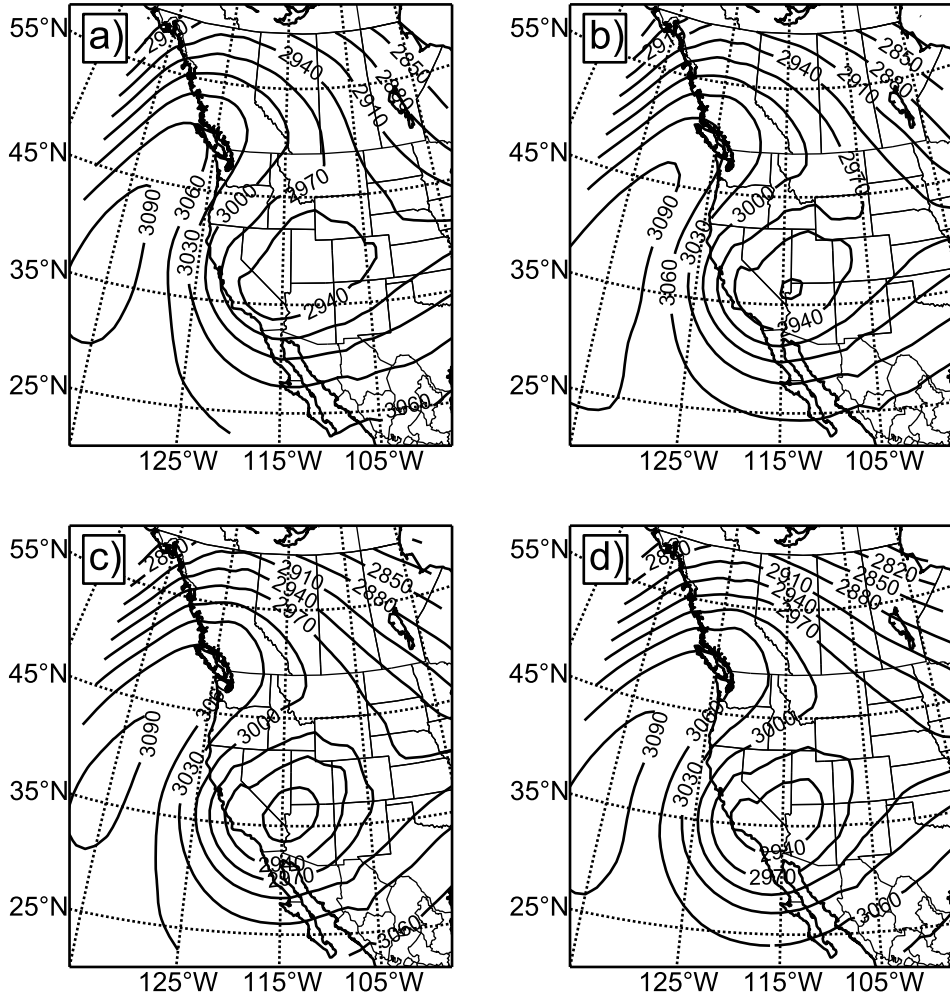


Figure 5: Evolution of ERA-Interim 700-hPa geopotential height (contoured at 30-m intervals), composited over 13 downslope windstorm events at (a) 0000 UTC, (b) 0600 UTC, (c) 1200 UTC, and (d) 1800 UTC

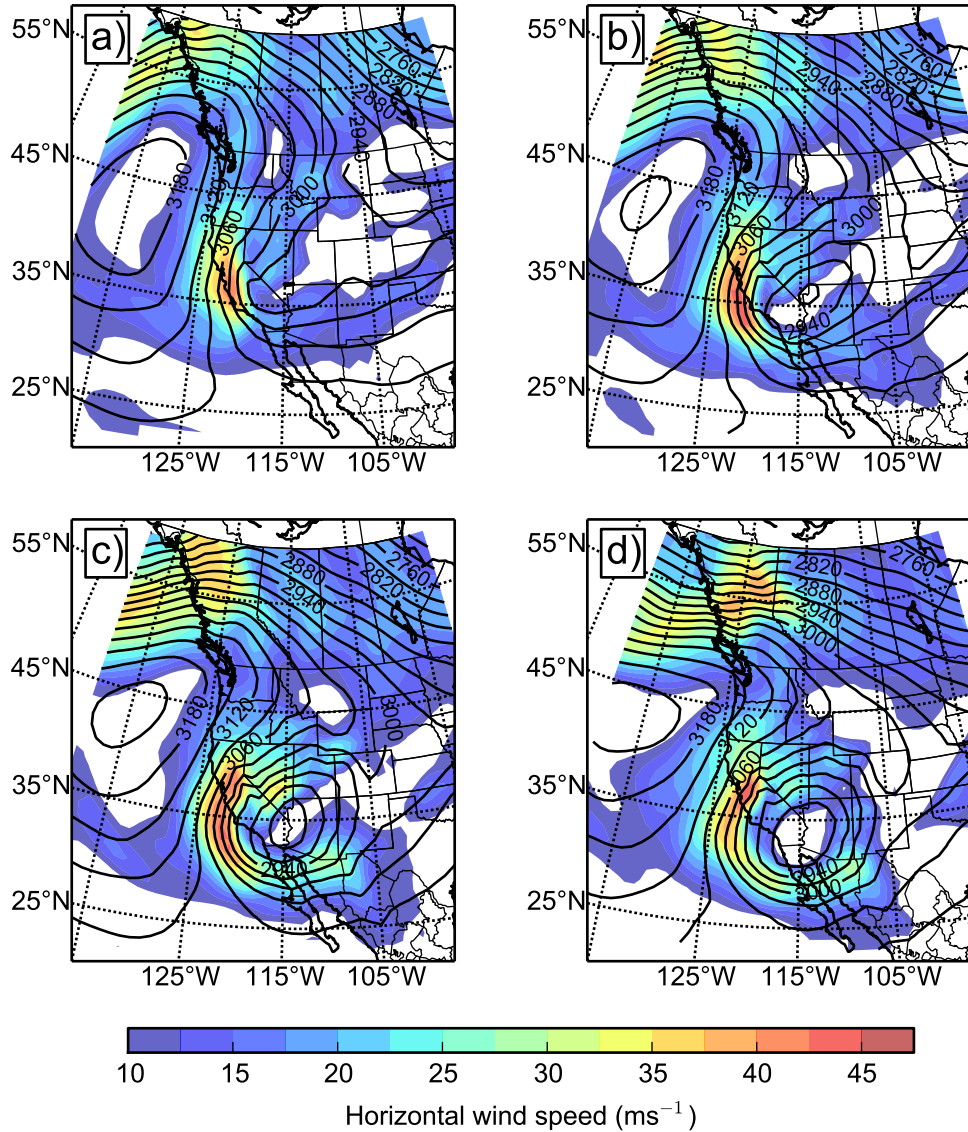


Figure 6: Evolution of 700-hPa geopotential height (contoured at 30-m intervals) and wind speed (shading according to scale) on 1 December 2011, taken from the ERA-Interim dataset, at (a) 0000 UTC, (b) 0600 UTC, (c) 1200 UTC, and (d) 1800 UTC..

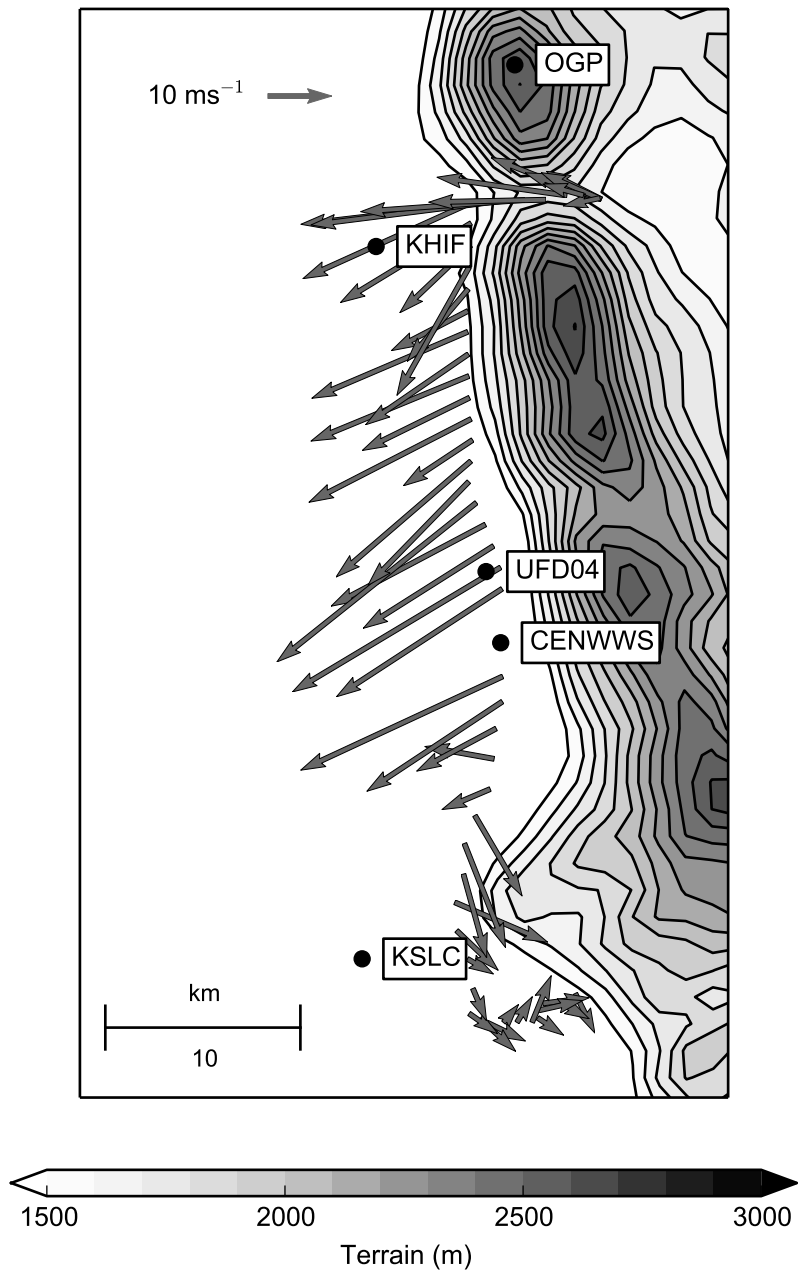


Figure 7: Mobile wind observations from 0915–1015 UTC. Vector arrows are relative to scale in top-left. Distance is according to the scale in bottom-left. Filled contours indicate terrain, taken from innermost WRF domain, with scale at bottom. Observation stations mentioned in text are labelled.

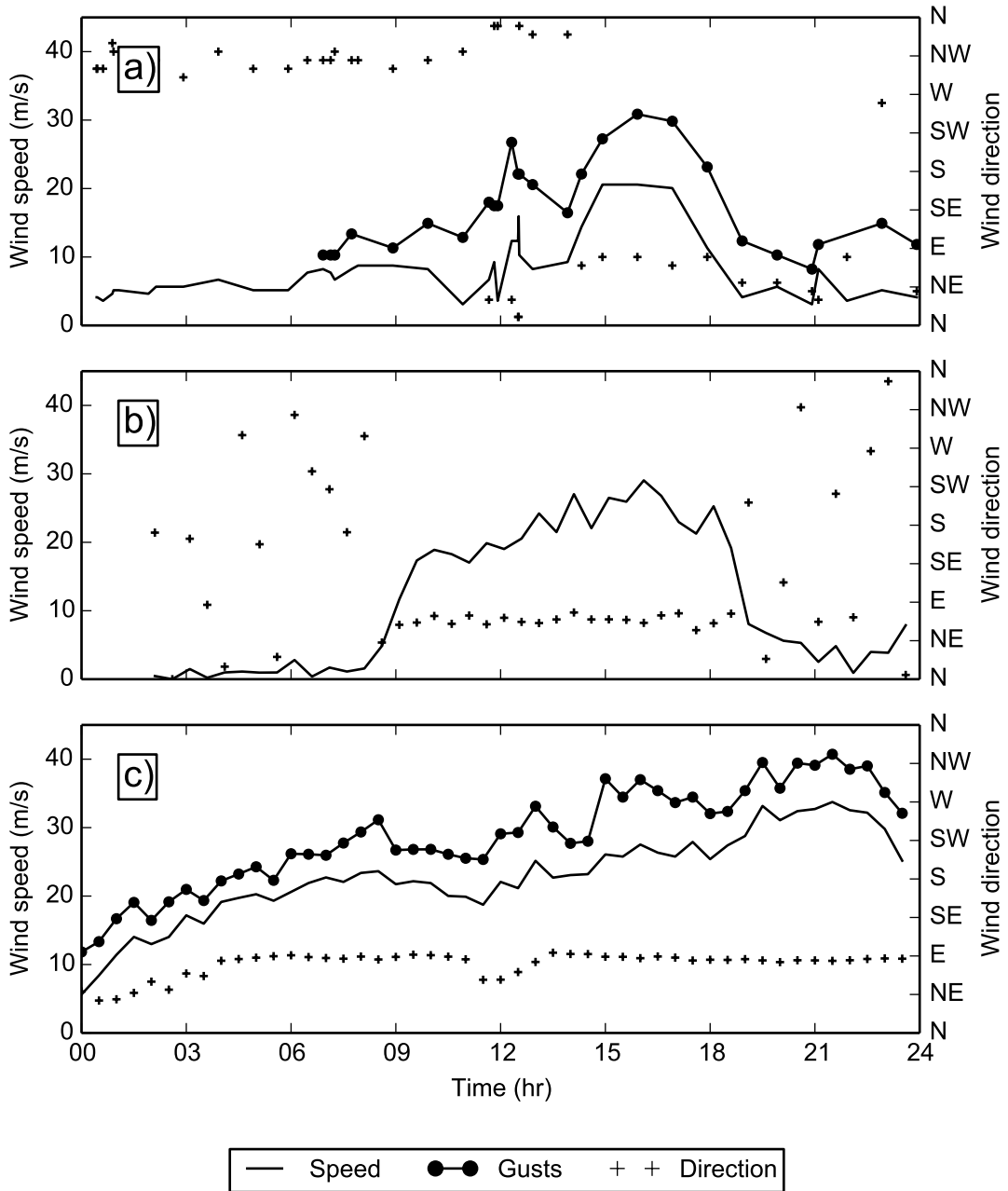


Figure 8: Surface wind observations at (a) Hill Air Force Base (KHIF), (b) Glover's Lane (UFD04), and (c) Ogden Peak (OGP) on 1 December 2011. Wind speed, wind gust, and wind direction shown by solid lines, filled circles, and crosses, respectively. All available KHIF observations are shown; for clarity, UFD04 and OGP data are sampled at 30-min intervals from the data available at higher reporting intervals.

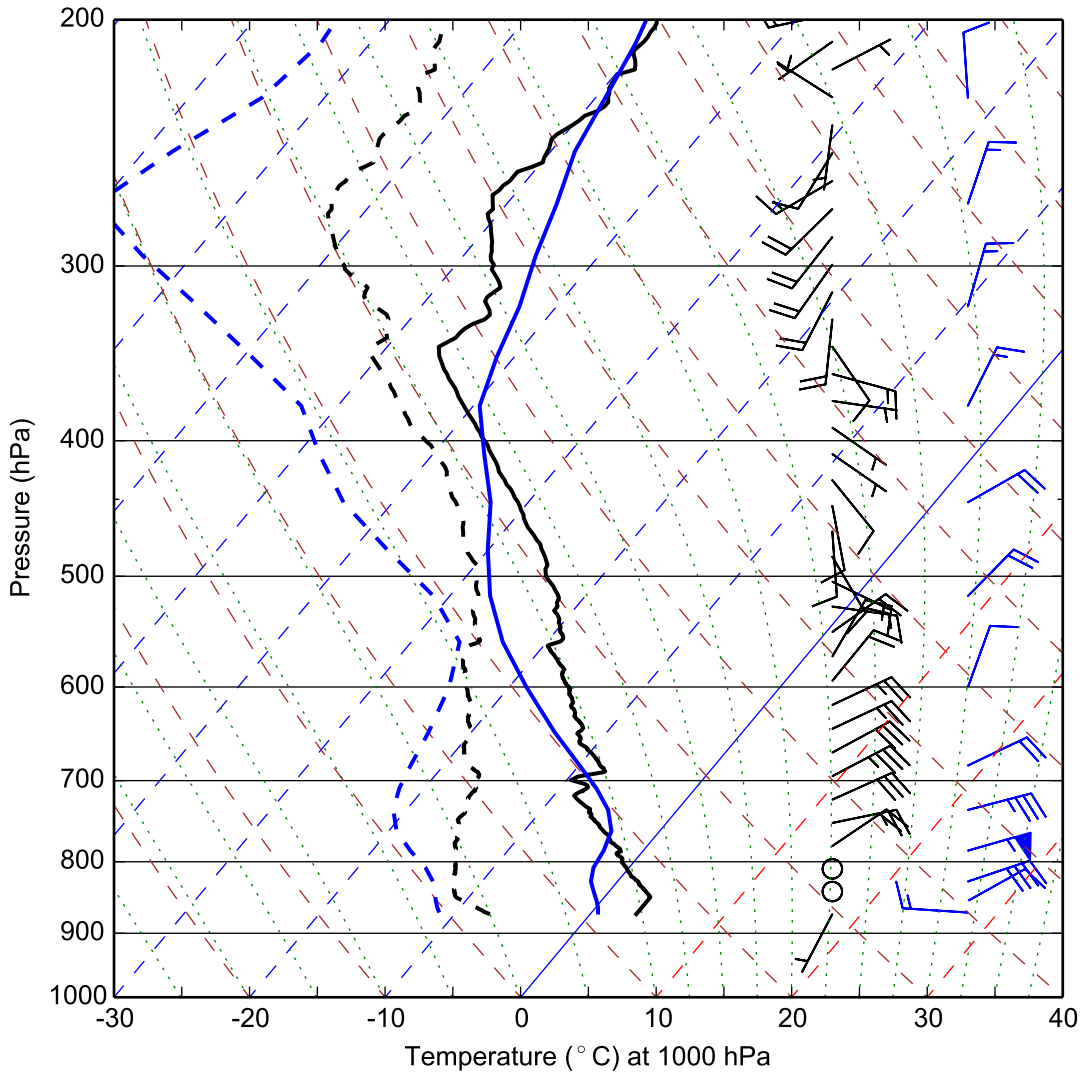
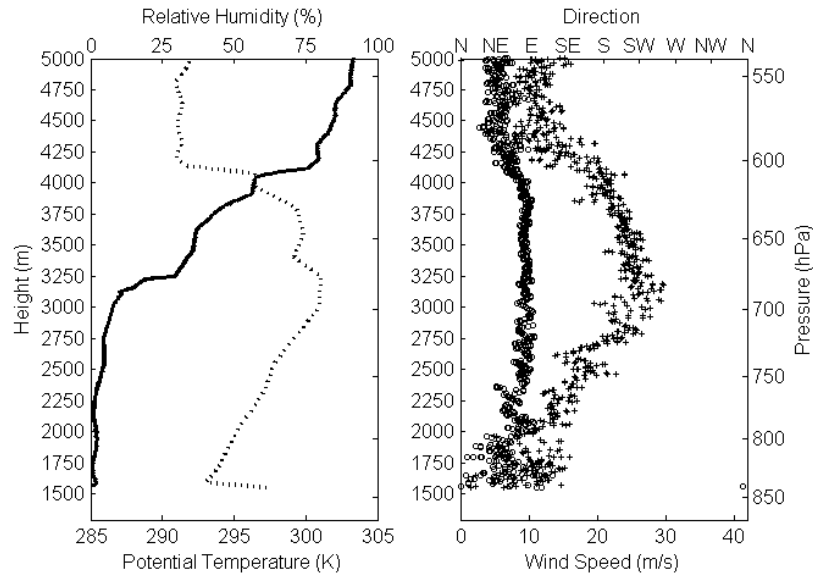
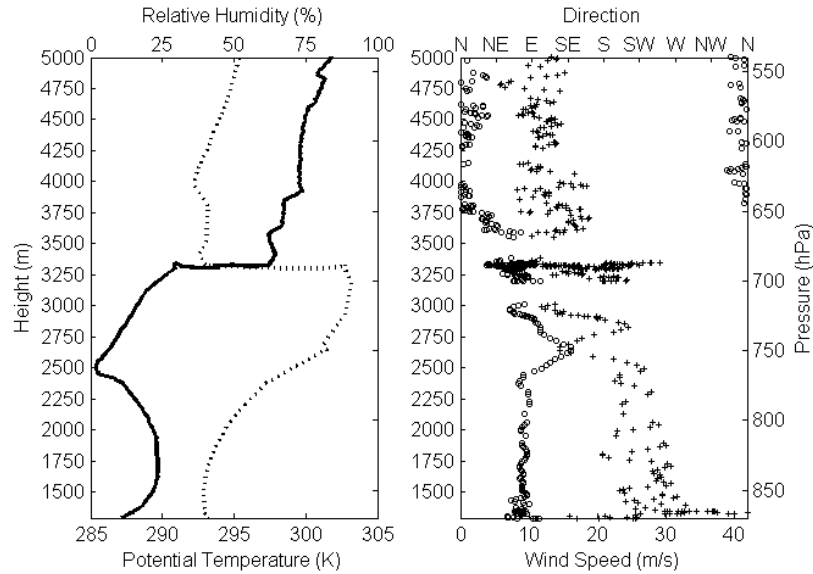


Figure 9: Skew-T log-P profiles at 1200 UTC 1 December 2011, from observed rawinsonde launch at KSLC (black lines) and from the WRF Control simulation at the nearest grid point (blue lines). Temperature, dew-point temperature, and wind denoted by solid lines, dashed lines, and barbs (full barb 5 m s^{-1}), respectively. For clarity, wind barbs from only selected model levels are shown.



(a) Morgan (UFD06)



(b) Centerville

Figure 10: Vertical profiles of observed rawinsonde data near Morgan, UT, and Centerville, UT (near CENWWS). (a) Potential temperature (solid line), relative humidity (dashed line), wind speed (crosses), and wind direction (open circles) at Morgan, UT, at 1800 UTC 1 December 2011, as a function of height. (b) As in (a) but for the 1200 UTC Centerville, UT launch.

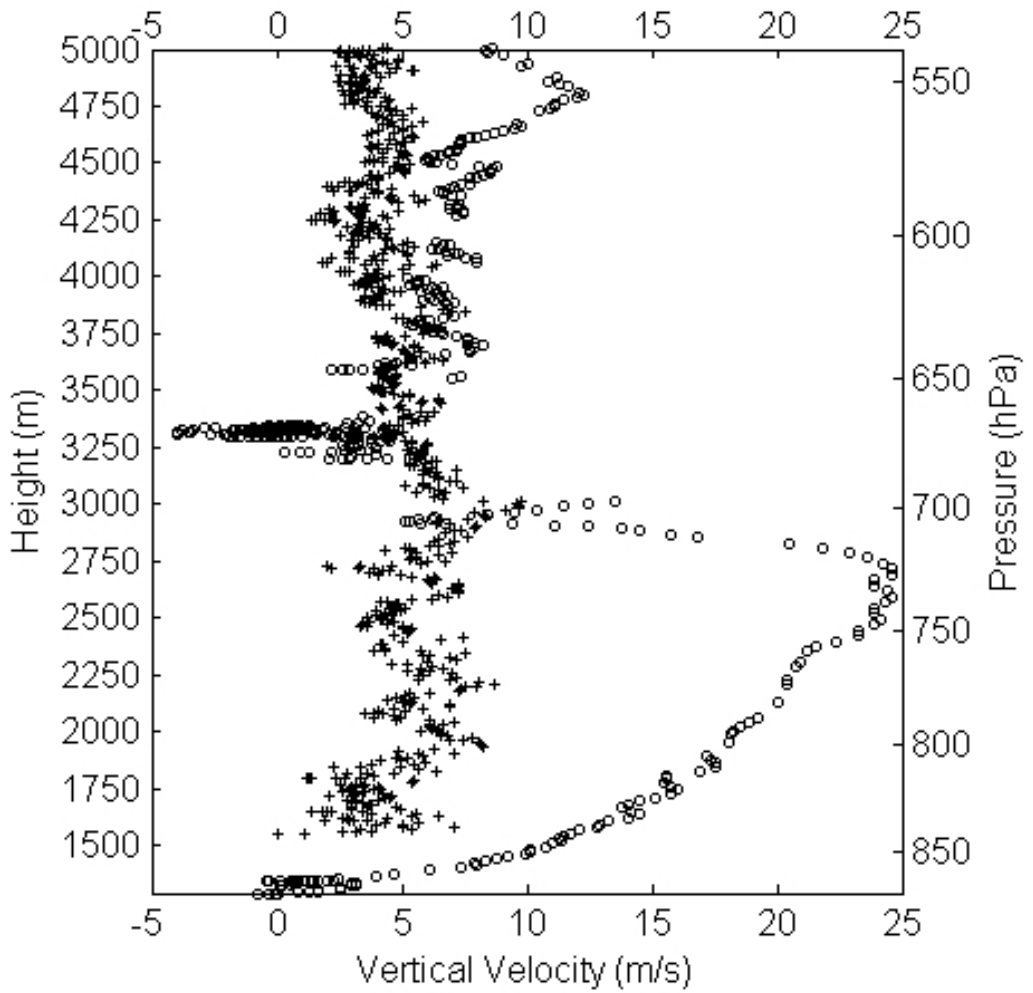


Figure 11: Comparison of rawinsonde ascent rates (m s^{-1}) at Morgan, UT (1800 UTC; crosses) and Centerville (1200 UTC; open circles).

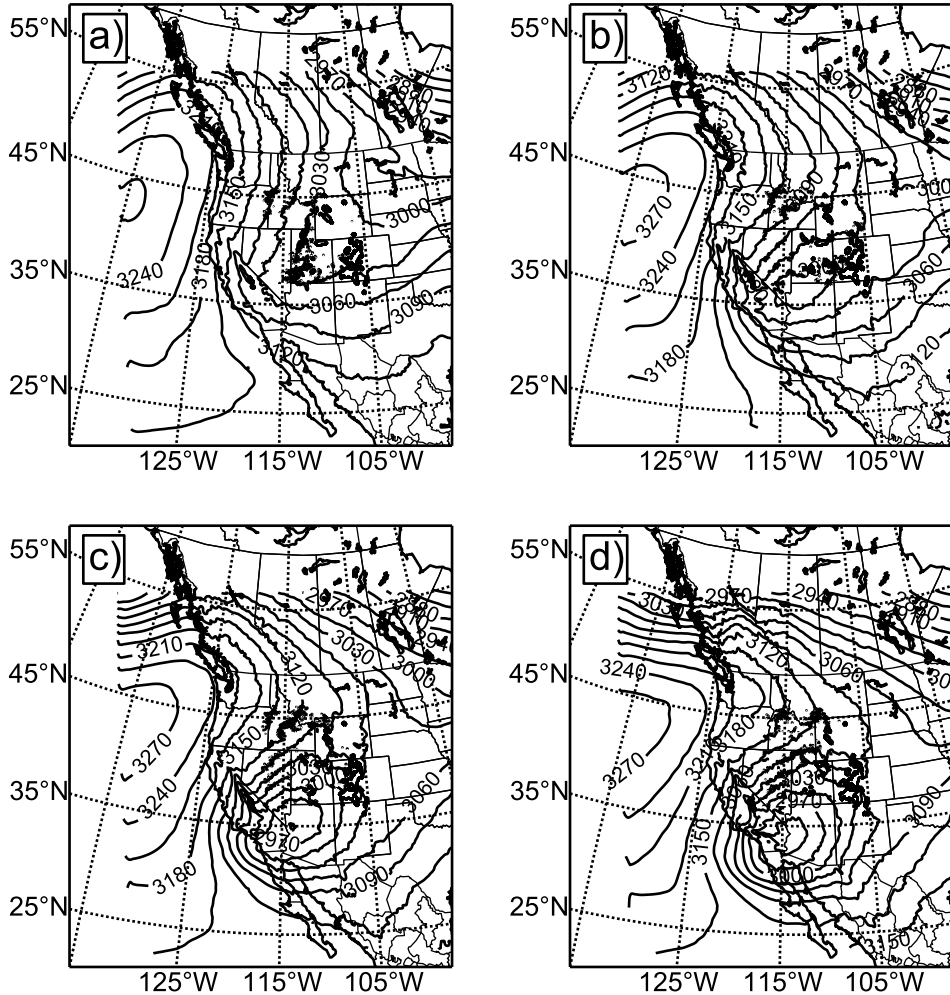


Figure 12: WRF Control simulation 700-hPa geopotential height fields (contoured at 30-m interval), at (a) 0000 UTC, (b) 0600 UTC, (c) 1200 UTC, and (d) 1800 UTC, all 1 December 2011. Noisy contours result from the 700-hPa surface intersecting the model terrain.

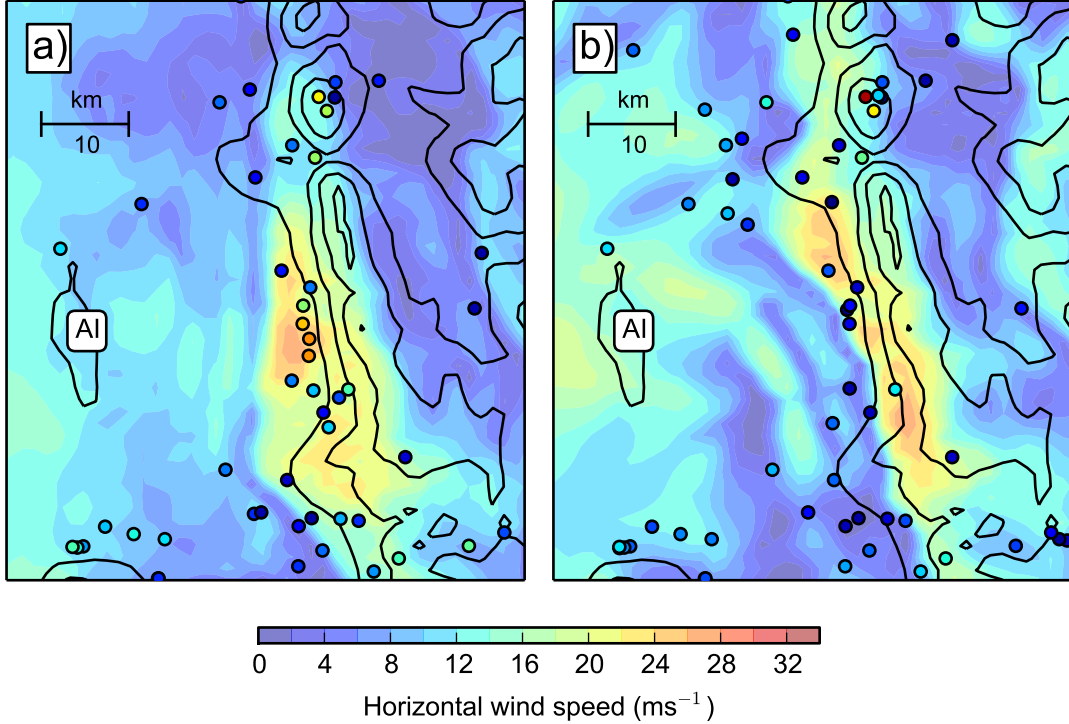


Figure 13: Comparison of observed surface wind speeds (colored circles) versus Control-simulation surface wind speeds (shading), both according to scale at bottom. The wind measurements are taken from the observation time closest to (a) 1200 UTC and (b) 2100 UTC, within 30 min either side of the respective times, for each available station. WRF innermost-domain terrain contoured every 400 m for reference; Antelope Island marked with “AI”.

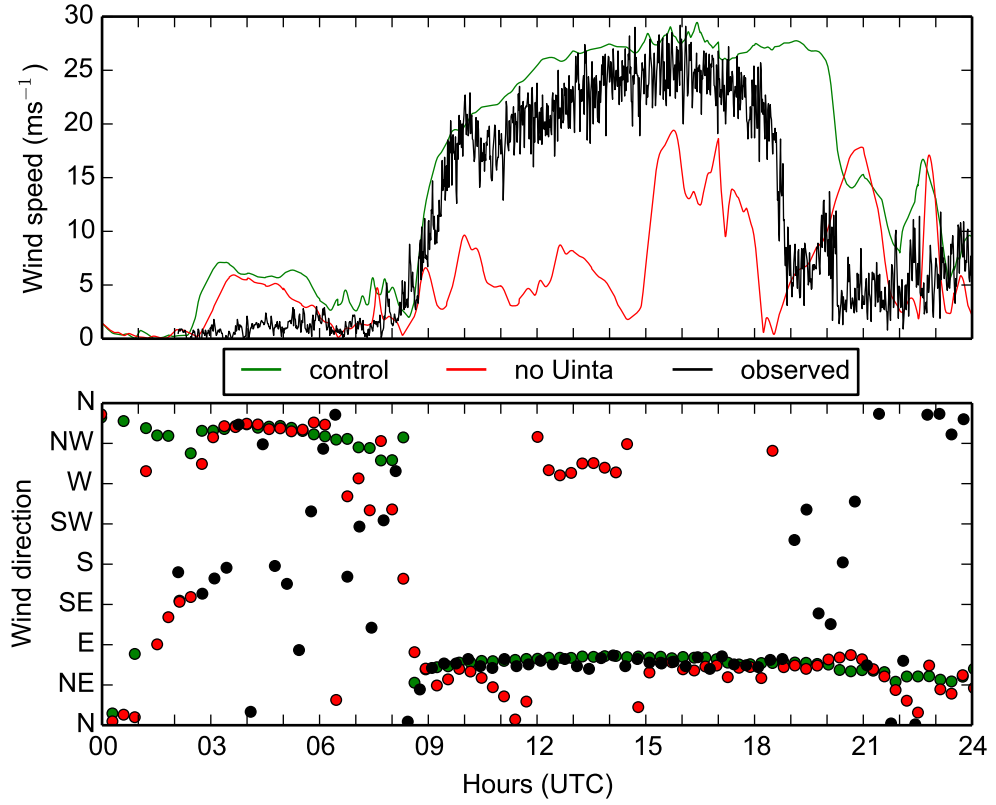


Figure 14: Observed and simulated surface winds at Glover's Lane (UFD04), UT on 1 December 2011. Observed wind speeds and wind directions from UFD04 are denoted by black solid lines and filled circles, respectively. Simulated surface wind speeds and directions from the Control (No-Uinta) simulations are shown by the green (red) solid lines and filled circles, respectively. Wind direction data from all three sources have been subsampled to every 20 minutes for clarity.

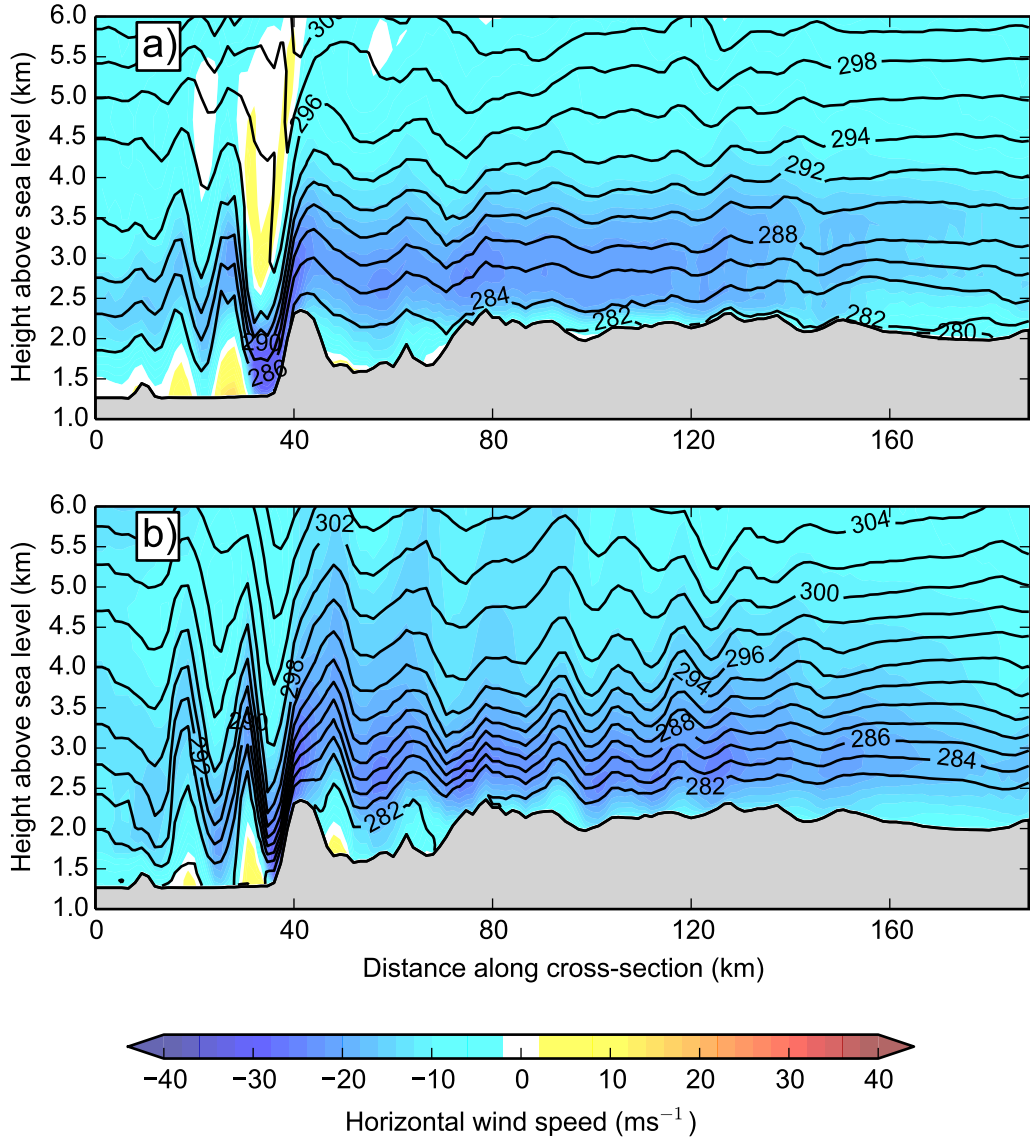


Figure 15: Perpendicular-to-Wasatch cross-section from innermost WRF domain (A–B in Fig. 1) at (a) 1200 UTC and (b) 2100 UTC, 1 December 2011. Shading denotes plane-parallel wind component according to the scale (e.g., blue indicates flow from right to left), while potential temperature is contoured at an interval of 2 K.

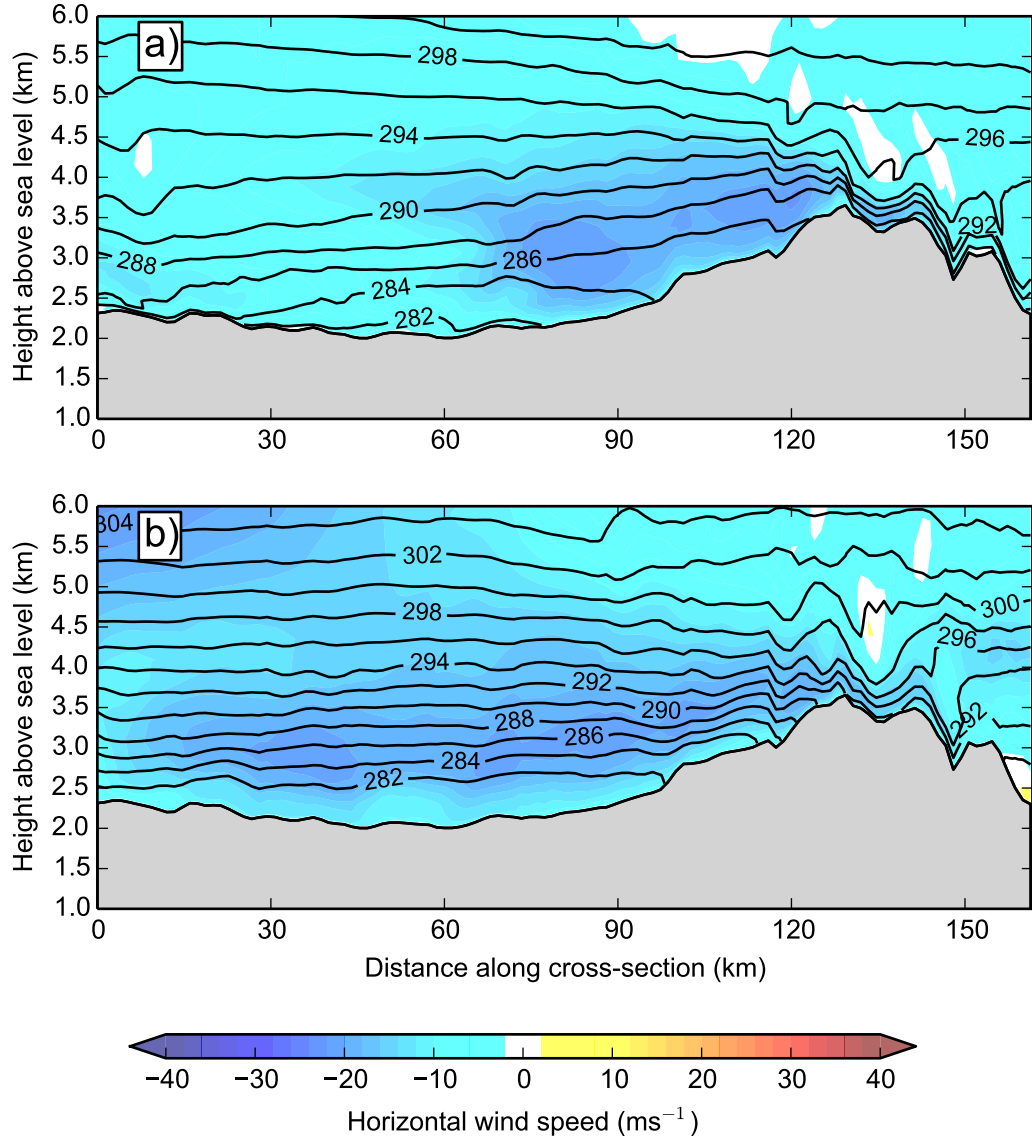


Figure 16: Roughly north–south cross-section from innermost WRF domain (C–D in Fig. 1) through west-central Wyoming (left) to the southern slopes of the Uintas (right) at (a) 1200 UTC and (b) 2100 UTC, 1 December 2011. Shading denotes wind component in and out of the page (e.g., blue indicates predominantly easterly flow out of the page) according to the scale; potential temperature is contoured at an interval of 2 K.

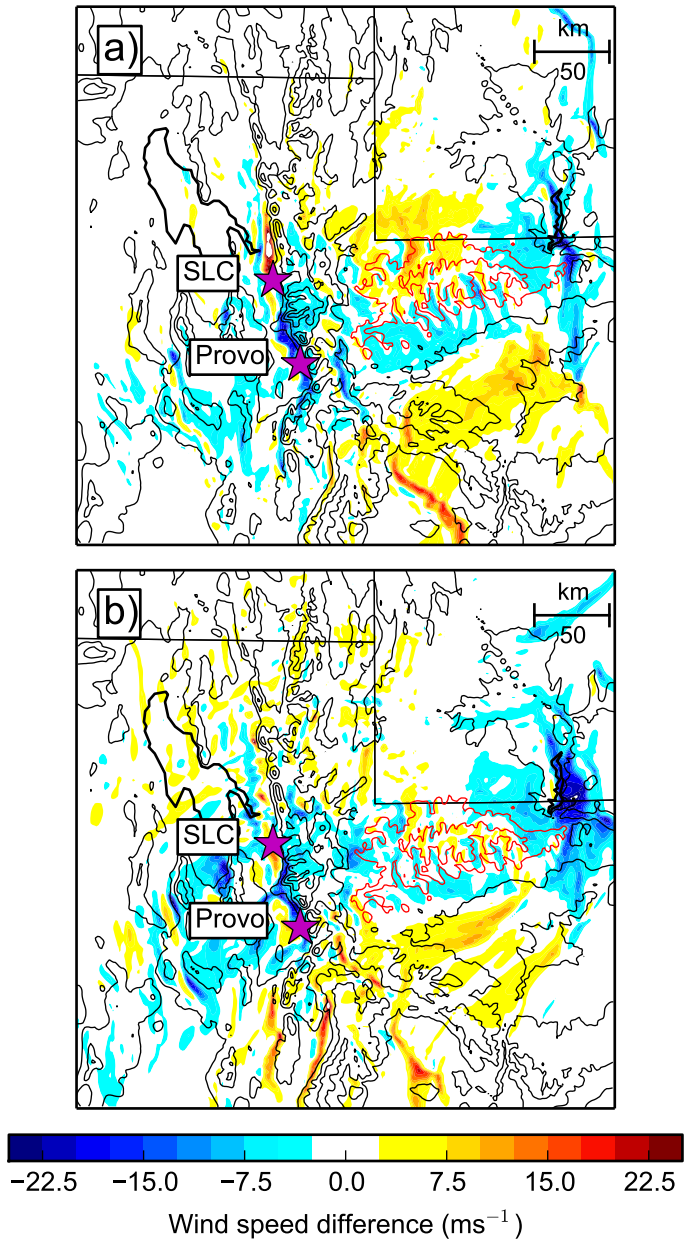


Figure 17: Zonal wind difference (No-Uinta minus Control), shaded according to the scale at the bottom, at (a) 1200 UTC and (b) 2100 UTC, 1 December 2011. Black (red) contours at 500-m intervals denote the elevation of the terrain used in both the Control and No-Uinta (Control only) simulations. Blue (red) indicates an increase (decrease) in easterly wind in this location as a result of removing the Uinta mountains.

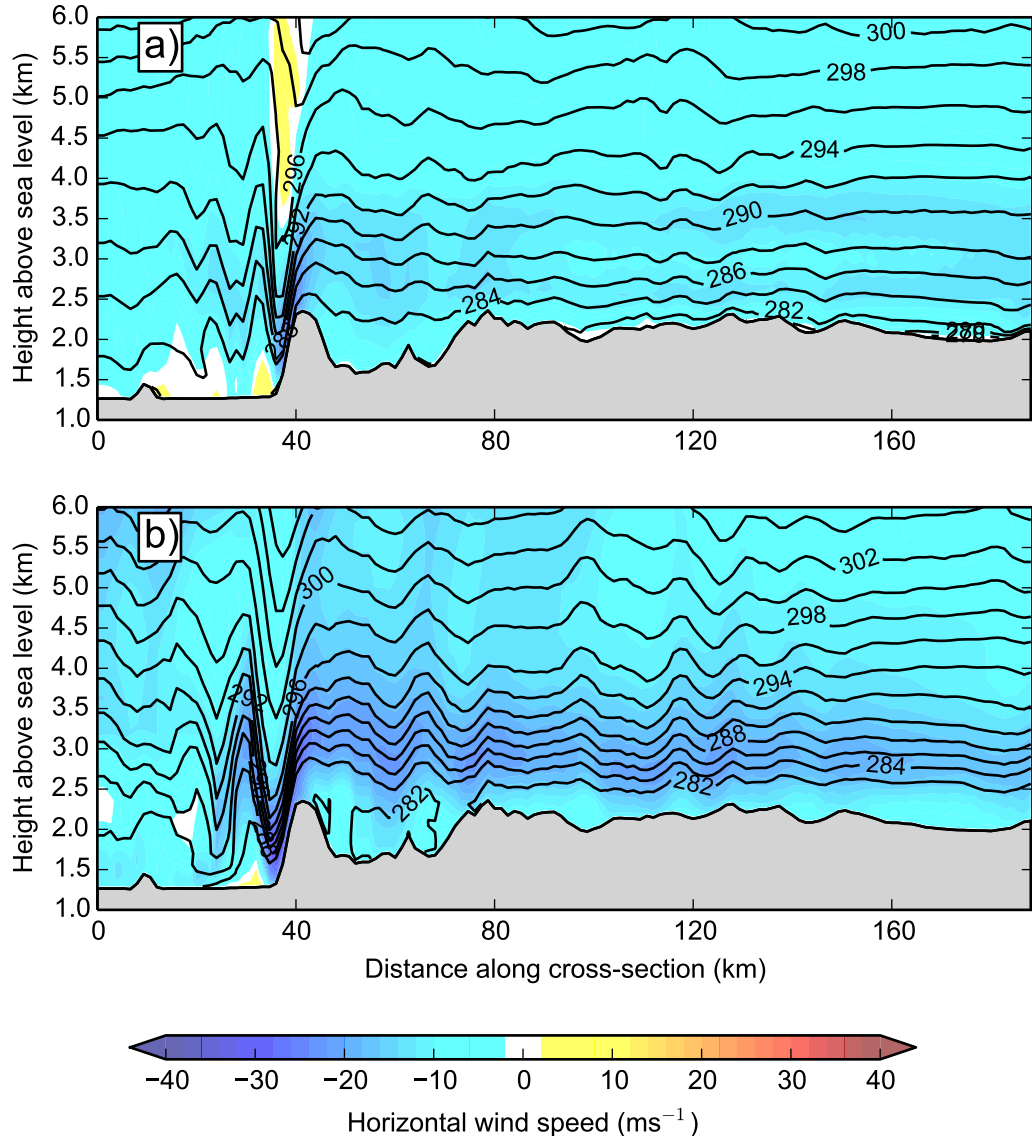


Figure 18: As in Fig. 15, but from the no-Uinta WRF simulation.

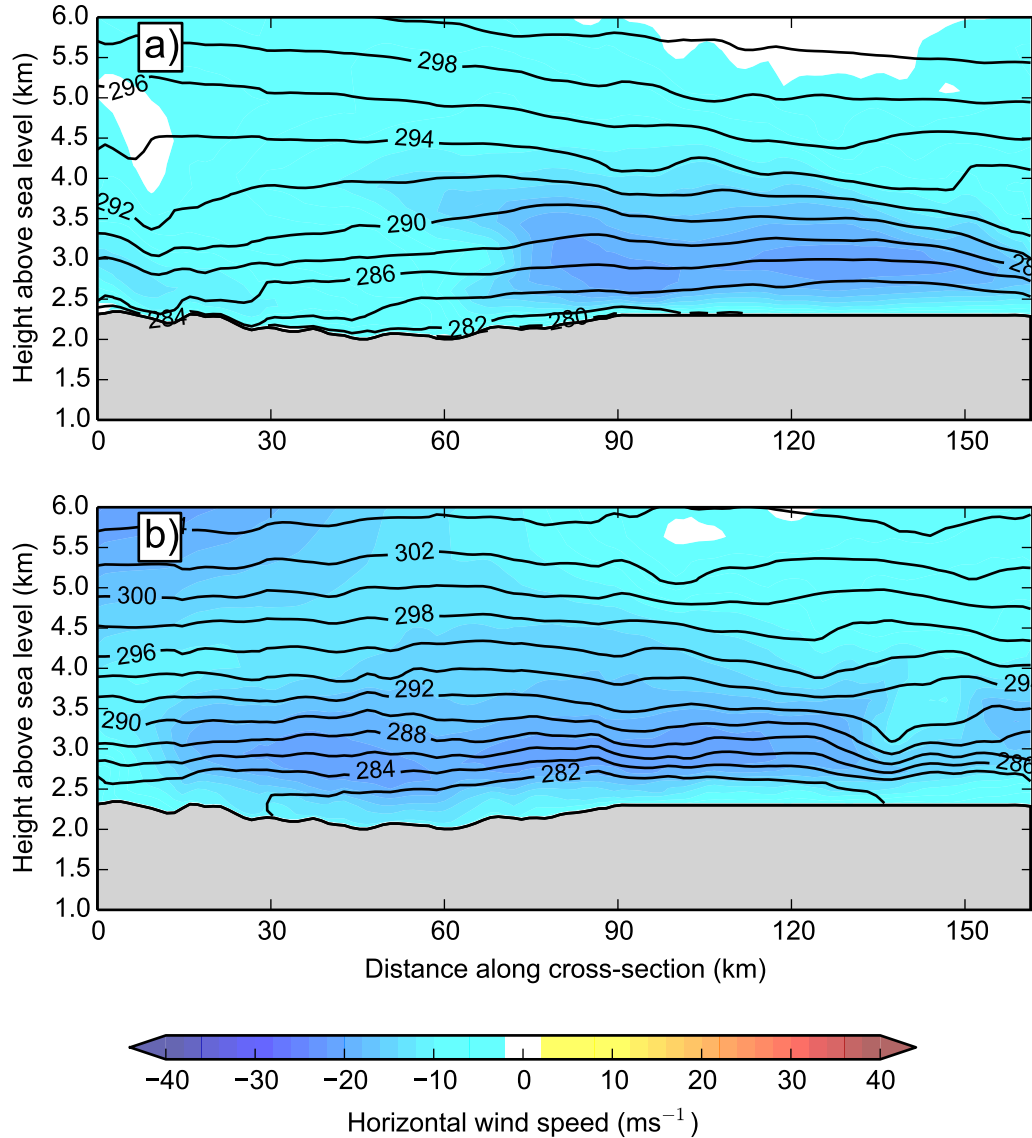


Figure 19: As in Fig. 16, but from the no-Uinta WRF simulation.